## Title

Generation of ultra-broadband, mid-IR radiation in GaAs pumped by picosecond 10 μm laser pulses

**Author**

Pigeon, Jeremy

**Publication Date**

2014

UNIVERSITY OF CALIFORNIA

Los Angeles

# Generation of ultra-broadband, mid-IR radiation in GaAs pumped by picosecond 10 μm laser pulses

A thesis submitted in partial satisfaction of the requirements for the degree of Master of Science in Electrical Engineering

By

Jeremy James Pigeon

2014

# ABSTRACT OF THE THESIS

# Generation of ultra-broadband mid-IR radiation in GaAs pumped by picosecond 10 μm laser pulses

By

Jeremy James Pigeon

Master of Science in Electrical Engineering

University of California, Los Angeles, 2014

Professor Chandrashekhar Joshi, Chair

Production of ultra-broadband radiation in the "molecular fingerprint region", from 2 – 20 μm is of practical interest for applications in optical coherence tomography, broadband spectroscopy and LIDAR measurements of gases. To date, supercontinuum generation in optical fibers has been limited to ~ 4.5 μm in the mid-IR range. In this thesis we describe an experiment in which supercontinuum radiation from 2 – 20 μm is generated using a 67 mm GaAs crystal pumped with a train of picosecond $CO_2$ laser pulses. In addition to spectral measurements, we have measured the temporal profile of the laser pulse after the interaction and observed splitting of the picosecond pulses into finer structure. Simulation show that such temporal structure may arise from modulational instability. Simulations further indicate that the observed spectral width is strongly influenced by stimulated Raman scattering and the use of a train of picosecond $CO_2$ laser pulses.

The thesis of Jeremy James Pigeon is approved.

Oscar Stafsudd

Warren B. Mori

Chandrashekhar Joshi, Committee Chair

# Dedication

To my family and friends, thank you for your support and understanding.

**Contents**

**List of Figures**

## List of Tables

# ACKNOWLEDGEMENTS

This project would have not been possible without the expertise of Dr. Sergei Tochitsky who conceived of the experiment and guided every aspect of this work. I would also like to thank Chao Gong for assistance in running the experiment and Professor Chan Joshi for providing guidance and for supporting this research. Finally, I would like to thank the entire UCLA Laser Plasma group for thought provoking discussion and moral support.

This work was supported by U.S. Department of Energy grant DE-SC001006

# 1. INTRODUCTION

Lasers can generate optical radiation which is spatially and temporally coherent, bright and nearly monochromatic. However, some applications would benefit from a broad-band source of coherent optical radiation. Such applications include: optical coherence tomography, broad-band spectroscopy, and optical pulse compression down to a few cycles of the electric field [1].

There are a variety of techniques to broaden the bandwidth of optical radiation while retain its spatial and temporal coherence. These techniques all involve nonlinear optical processes, that is, processes where the refractive index of a medium depends on the intensity of the light passing through. When some of these processes are used to generate spatially coherent radiation with a bandwidth comparable to the laser's carrier frequency these schemes are called supercontinuum (SC) generation [1].

Supercontinuum generation was first observed in fused silica in 1970 by Alfano and Shapiro using a picosecond, Nd:Glass laser[2]. Since then SC generation has been the subject of active investigation in solids, gases and liquids using a variety of pump sources, materials, and nonlinear processes. Due to the number of techniques to generate SC, it is instructive to classify SC generation experiments in two regimes: the high field (intensity, $I \geq 10^{11} W/cm^2$) and low field ($I \leq 10^{10} W/cm^2$) regime.

In the high field regime the observed SC spectra is broadened to approximately $\frac{\Delta\nu}{\nu_0} \approx 10^{-1}$ and is characterized by a spectral power density which drops off very rapidly as one moves away from the carrier frequency. In these experiments the spectral broadening is due to self-phase modulation (SPM), laser filamentation and plasma formation [1]. In this high field regime the laser intensity exceeds the damage threshold of the solid medium and, as a result, these experiments tend to involve SC generation in gases.

The most successful SC sources operate in the low field regime and are based on optical fibers. Unlike the high field regime, SC generation in fibers is attributed to a dynamic interplay between Stimulated Raman scattering (SRS), parametric four-wave mixing (FWM) and, when the pump's wavelength lies in the anomalous dispersion regime, modulational instability (MI). In these experiments self-phase modulation plays a minor role, mainly acting to seed the onset of MI. Due to the interplay between these processes, the observed spectral power density in these experiments is incredibly broad with $\frac{\Delta\nu}{\nu_0} \geq 1$, an order of magnitude greater than in the high intensity regime. In both the high and low field regimes the vast majority of SC generation research involves radiation generation in the region from ~ 0.8 – 2 μm, where high power pump lasers are available.

In general there is a strong desire to produce a SC source which covers 2 – 20 μm, the "molecular fingerprint" region of the electromagnetic spectrum, so called because all molecules have a resonant vibrational-rotational response at one or more of these wavelengths. The most successful attempt to cover this region was obtained through the use of a meter scale photonic crystal fiber (PCF) pumped by nanosecond diode laser pulses [3]. In this experiment, the researchers observed a long-wavelength plateau which extended to 4.5 μm, a cut-off determined by the opacity of the nonlinear medium. It should be mentioned that there are materials, such as GaAs or CdTe, which have excellent nonlinear properties for SC generation. GaAs, for example, has suitable dispersion and a nonlinear index of refraction 1000 times that of fused silica. In principle, this incredibly high nonlinearity could be used to produce a comparable broadening as observed in meter scale fibers albeit in a much shorter, centimeter scale, interaction length. Unfortunately, these materials are opaque in the near-IR and have seen limited use due to the lack of a suitable pump.

A picosecond carbon dioxide laser, lasing at 10 μm, is an obvious candidate for the generation of SC in GaAs. To the author's knowledge there is only one experiment in the literature which involves generating mid-IR supercontinua in a 7 cm GaAs crystal pumped by a $CO_2$ laser [4]. Here researchers observed a SC spanning 3 – 14 um after tightly focusing a single, 600 μJ, 2.5 ps pulse to an intensity of $\sim 10^{11} \frac{W}{cm^2}$. Due to the high intensity yet low peak power of their laser, the resulting spectrum is dominated by SPM characteristic to the high field regime. Although the researchers observed Raman components in the SC spectra they failed to produce bandwidth as broad as more recent SC generation experiments in photonic crystal fibers [3].

In this thesis we describe experiments in which we explore the possibility of generating a SC by sending a train of 2-5 GW, 3 ps $CO_2$ laser pulses through a ~ 7 cm long GaAs crysal. We focus the beam to an intensity of $\approx 10^{10} W/cm^2$ in order to remain below the damage threshold of the material and to efficiently pump the crystal. Due to these pulse parameters we observe a significant Raman contribution and an unprecedentedly broad SC spectrum which covers 2 – 20 μm. We have also measured the temporal structure of our pulses after the interaction showing that the observed spectral broadening is consistent with the onset of a modulational instability that produces individual pulse splitting in the time domain.

## 2. THEORY

### 2.1 The Nonlinear Index of Refraction

If the driving optical field strength is on the order of the field which binds the electron to the nucleus ($\sim 10^9\ V/m$) then the response from the medium becomes nonlinear and can be approximated as a power series:

$$\vec{P}(\vec{r},\omega) = \vec{P}^{(1)}(\vec{r},\omega) + \vec{P}^{(2)}(\vec{r},\omega) + \vec{P}^{(3)}(\vec{r},\omega) + \cdots \tag{1}$$

If we express the total polarization in terms of the electric field then Eq. (1) takes the form of

$$\vec{P}(\vec{r},\omega) = \epsilon_0\{\overleftrightarrow{\chi}^{(1)} \cdot \vec{E}(\vec{r},\omega) + \overleftrightarrow{\chi}^{(2)} \cdot \vec{E}(\vec{r},\omega)\vec{E}(\vec{r},\omega) + \overleftrightarrow{\chi}^{(3)} \cdot \vec{E}(\vec{r},\omega)\vec{E}(\vec{r},\omega)\vec{E}(\vec{r},\omega) + \cdots\} \tag{2}$$

In general the $n^{th}$ order susceptibility is a complex valued tensor of order n. In centrosymmetric media the even order susceptibilities vanish and the susceptibilities are reduced to scalars, in this case it is convenient to focus on the largest non-vanishing term, the third order polarization and define a nonlinear index of refraction:

$$n = n_0 + n_2 I \tag{3}$$

Where the nonlinear index , $n_2$, is related to the third order susceptibility by $n_2 = \frac{3}{4}\chi^{(3)}$. The nonlinear index is expressed in units of $\frac{cm^2}{W}$ and can vary by six or more orders of magnitude between different materials. For example, the nonlinear index of refraction of GaAs is one million times larger than the nonlinear index of the air and about one thousand times larger than that of fused silica.

## 2.2 Dispersion and Group Velocity

Dispersion, a consequence of causality, is present whenever a medium has a non-negligible response time and is used to describe how the index of refraction changes with the frequency of the driving electric field. It is customary to express the material's dispersion by considering that the propagation constant varies as a function of frequency, $\beta(\omega)$, where $n = \frac{c\beta}{\omega}$. Since a material's dispersion across an arbitrary frequency range is typically unknown it is common to express the function as a Taylor series expanded around the central frequency, $\omega_0$,

$$\beta(\omega) = \beta_0 + \beta_1(\omega - \omega_0) + \frac{1}{2}\beta_2(\omega - \omega_0)^2 + \cdots \tag{4}$$

In the above we use $\beta_m = \partial^m \beta / \partial \omega^m$. The first term of the expansion, $\beta_1$ ,is the reciprocal of the pulse's group velocity. The second term, $\beta_2$, is the term responsible for group velocity dispersion (GVD). Spectral regions with positive $\beta_2$ values are defined to have normal GVD while regions with a negative $\beta_2$ have anomalous GVD. In the normal GVD regime high frequency radiation travels slower than low frequency radiation while in the anomalous regime the opposite is true. In between regions of negative and positive GVD there is a so-called zero dispersion wavelength (ZDW) where $\beta_2$ becomes zero. In fused silica the ZDW point is near 1 um while in GaAs the ZDW point is near 7 um. As we will see in the forthcoming chapters, the dispersion of the nonlinear medium, specifically whether $\beta_2$ is positive or negative, is one of the most important parameters in predicting what will happen in very broad band, nonlinear optical processes.

## 2.3 Summary of Third Order Processes Responsible for Supercontinuum Generation

In this section we summarize all of the third order nonlinear optical processes which lead to supercontinuum generation. In GaAs the following third order effects are all occurring simultaneously: Self-phase modulation, Stimulated Raman Scattering, four wave mixing, modulational instability and third harmonic generation. As an illustrative example, third harmonic generation can be expressed as:

$$\vec{P}^{(3)}(3\omega_0) = {\chi'}^{(3)}(3\omega_0 = \omega_0 + \omega_0 + \omega_0) \cdot \vec{E}(\omega_0)\vec{E}(\omega_0)\vec{E}(\omega_0) \quad (5)$$

which shows, in the argument of the susceptibility, which frequencies are being mixed to produce the newborn radiation. Since the susceptibility is a complex value it must be expressed as, $\chi = \chi' + i\chi''$, where the single prime indicates the real part of the susceptibility and the double prime indicates the imaginary part. Processes which rely on the real part of the susceptibility are referred to as parametric processes while processes which rely on the imaginary part of the susceptibility are referred to as nonparametric processes [7].

The most practically important difference between parametric and nonparametric processes involves what is known as phase matching. For efficient interaction, parametric processes must be properly phase matched while there is no such requirement for nonparametric processes since they interact with an active medium. Phase matching is achieved by satisfying conservation of photon energy and momentum, using the example of third harmonic generation the phase matching criteria are:

$$3\omega_0 = \omega_0 + \omega_0 + \omega_0 \quad (6a)$$

and,

$$\vec{\beta}(3\omega_0) = \vec{\beta}(\omega_0) + \vec{\beta}(\omega_0) + \vec{\beta}(\omega_0). \quad (6b)$$

| | |
|---|---|
| Third harmonic generation | $\mathbf{P}(3\omega_0) = \epsilon_0 \chi'^{(3)}(3\omega_0 = \omega_0 + \omega_0 + \omega_0) \cdot \boldsymbol{E}(\omega_0)\boldsymbol{E}(\omega_0)\boldsymbol{E}\,(\omega_0)$ |
| Stimulated Raman Scattering | $\mathbf{P}(\omega_S) = \epsilon_0 \chi''^{(3)}(\omega_S = \omega_S + \omega_0 - \omega_0) \cdot \boldsymbol{E}(\omega_S)\boldsymbol{E}(\omega_0)\boldsymbol{E}^*(\omega_0)$ |
| Parametric Raman Scattering | $\mathbf{P}(\omega_S) = \epsilon_0 \chi'^{(3)}(\omega_s = \omega_0 + \omega_0 - \omega_{AS}) \cdot \boldsymbol{E}(\omega_0)\boldsymbol{E}(\omega_0)\boldsymbol{E}^*(\omega_{AS})$ |
| Parametric Raman Scattering | $\mathbf{P}(\omega_{AS}) = \epsilon_0 \chi'^{(3)}(\omega_{AS} = \omega_0 + \omega_0 - \omega_S) \cdot \boldsymbol{E}(\omega_0)\boldsymbol{E}(\omega_0)\boldsymbol{E}^*(\omega_S)$ |
| Four-wave mixing | $\mathbf{P}(\omega_4) = \epsilon_0 \chi'^{(3)}(\omega_4 = \omega_1 + \omega_2 - \omega_3) \cdot \boldsymbol{E}(\omega_1)\boldsymbol{E}(\omega_2)\boldsymbol{E}^*(\omega_3)$ |
| Self-phase modulation | $\mathbf{P}(\omega_0) = \epsilon_0 \chi'^{(3)}(\omega_0 = \omega_0 + \omega_0 - \omega_0) \cdot \boldsymbol{E}(\omega_0)\boldsymbol{E}(\omega_0)\boldsymbol{E}^*(\omega_0)$ |
| Modulational instability* | $\mathbf{P}(\omega_{AS}) = \epsilon_0 \chi'^{(3)}(\omega_{AS} = \omega_0 + \omega_0 - \omega_S) \cdot \boldsymbol{E}(\omega_0)\boldsymbol{E}(\omega_0)\boldsymbol{E}^*(\omega_S)$ |
| Modulational instability * | $\mathbf{P}(\omega_S) = \epsilon_0 \chi'^{(3)}(\omega_s = \omega_0 + \omega_0 - \omega_{AS}) \cdot \boldsymbol{E}(\omega_0)\boldsymbol{E}(\omega_0)\boldsymbol{E}^*(\omega_{AS})$ |

Table 1: Summary of the third order nonlinear optical processes which occur in GaAs

Nonparametric processes do not require phase matching because the medium plays an active role in the interaction, that is, the response of the medium defines the phase of the outgoing radiation which guarantees that the interaction is phase matched.

Table 1 summarizes the pertinent third order nonlinear processes which occur in GaAs along with the photon frequencies involved in the interaction. Note that the processes which are listed in table 1 twice generate two frequencies which are symmetrically generated around the carrier. In this situation it is conventional to name the low frequency radiation “Stokes” and the high frequency radiation “anti-Stokes”. For clarity we have labeled the characteristic Raman related frequencies as $\omega_S$ and $\omega_{AS}$ and modulational instability frequencies as $\omega_L$ and $\omega_H$. The following sections of this chapter will be used to elaborate on the most important effects for the experiment described here: Self-phase modulation (SPM), stimulated Raman Scattering (SRS) and modulational instability (MI).

## 2.4 Self-phase Modulation

An intensity dependent refractive index combined with a laser pulse of finite temporal duration and sufficiently high intensity results in self-phase modulation. The easiest way to understand this fact is by examining the total phase argument of a plane electromagnetic wave in one dimension, assuming a field of the form $E = E_0\cos(\phi(x,t))$, the phase is:

$$\phi(x,t) = \omega_0 t - \beta x \tag{7}$$

Where $\beta = \frac{n\omega_0}{c} = \frac{(n_0+n_2 I(t))\omega_0}{c}$ and $I(t) = I_0\exp(-\frac{t^2}{\tau^2})$. By using the definition of instantaneous frequency we can now analyze what would happen if the pulse was sent through a nonlinear medium,

$$\omega_i(t) = \frac{\partial\phi}{\partial t} = \omega_0 - \frac{n_2\omega_0}{c}(\frac{\partial I}{\partial t})x \tag{8}$$

The physical interpretation of Eq. 8 is straight forward. When we allow for a nonlinear index of refraction and a finite laser pulse, we find that the instantaneous frequency changes in proportion to the derivative of the pulse's intensity. As can be seen by examination of Eq. 8, the leading edge of the pulse creates long wavelength radiation while the falling edge of the pulse creates short wavelength radiation. This effect changes the pulse in two ways, first by increasing the pulse's bandwidth and second by creating a chirp across the pulse.

We can estimate the total amount of bandwidth gained using SPM from Eq. 8 for the peak of the lasers intensity $\Delta\omega \approx 2\frac{n_2\omega_0 I_0 L}{c\tau}$. Unlike the majority of SC radiation, bandwidth created through SPM has a nearly linear chirp and, as a consequence, be compressed with the use of gratings or a material with anomalous GVD. This technique has been used to compress pulses down to a single cycle of the optical field [5].

## 2.5 Stimulated Raman Scattering

Stimulated Raman Scattering is a process by which an electromagnetic field can couple with quantum vibrations in a medium. This coupling is usually observed as downshifting of the carrier frequency where, as described in the previous section, the downshifted light is referred to as the Stokes signal.

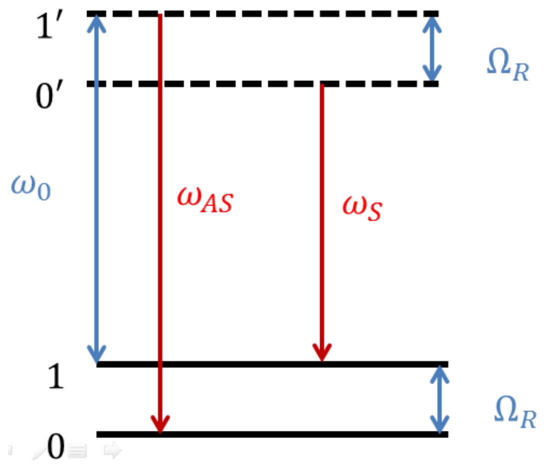

Figure 1: Energy level diagram of the Raman scattering process. Here the prime indicates a virtual level.

Physically this process can be understood as an inelastic collision between the photon and the medium, after the collision the photon loses some energy which, in crystals, is carried away in the form of an optical phonon. Figure 1 shows an energy level diagram which qualitatively illustrates this process. When the driving field is incident on the material, it may excite a virtual transition which can absorb some energy from the photon. The reverse process, a phonon delivering energy to the incident photon, is possible but less likely due to the fact that a phonon must already be in place before the photon arrives. In general one observes both Stokes and anti-stokes light which are related to the Raman frequency by $\omega_{\frac{S}{AS}} = \omega_0 \mp \Omega_R$ where $\Omega_R$ is the Raman frequency. The Raman scattering process is central in modern studies of SC generation. In fact it is the nonlinear coupling between SRS and FWM which causes such broadband light to be generated in recent SC experiments [3].

## 2.6 Modulational Instability

Modulational instability (MI) in an optical fiber was first observed in 1986 by Tai, Hawegawa and Tomita and is described as amplitude and phase modulation of an input laser pulse as a result of coupling between nonlinearity and anomalous dispersion [6]. A laser pulse subjected to a modulational instability develops symmetric lobes at $\pm n\Omega_{MI}$ where $n$ is a positive integer and $\Omega_{MI}$ is a frequency determined by the maximum of the modulational instability gain spectrum. In the time domain this process manifests as an ultrafast modulation which splits a laser pulse into a train of fundamental solitons. The result of MI can also be interpreted as four-wave mixing. In this view, two pump photons annihilate to form a frequency downshifted and upshifted photon, similar to the language used to describe this interaction in figure (1).

The gain spectrum of the modulational instability is given by [7]:

$$g(\Omega) = |\beta_2\Omega|(\Omega_c^2 - \Omega^2)^{\frac{1}{2}}. \tag{9}$$

Where the maximum gain is found at $\Omega_{max} = \pm\frac{\Omega_c}{\sqrt{2}} = \pm\left(\frac{2\gamma P_0}{|\beta_2|}\right)^{\frac{1}{2}}$ which defines the periodicity of the pulse train in the time domain as $\frac{2\pi}{\Omega_{max}}$ [7]. By inspection of Eq. 9 we see that, as pump power increases, the maximum frequency shift increases which, in turn, create faster pulses in the time domain.

## 2.7 The Nonlinear Schrödinger Equation

Reduction of Maxwell's Equations yields a nonlinear wave equation governing the evolution of an envelope of an optical pulse. This equation has been widely studied and is referred to as the Nonlinear Schrödinger Equation (NLS), in the formalism used by the nonlinear fiber optics community the NLS takes the form of [7]:

$$\frac{\partial A}{\partial z} + \beta_1\frac{\partial A}{\partial t} + \frac{i\beta_2}{2}\frac{\partial^2 A}{\partial t^2} + \frac{\alpha}{2}A = i\gamma|A|^2 A \tag{10}$$

Where A is related to the complex electric field amplitude by $\tilde{E}(\vec{r},\omega) = F(x,y)\tilde{A}(z,\omega)\exp(i\beta_0 z)$, and the function $F(x,y)$maps the spatial distribution of the beam. The units of A are $W^{\frac{1}{2}}$ so that $|A|^2$ corresponds to the instantaneous power in the pulse. In Eq. 10, $\alpha$ is the linear loss coefficient and,

$$\gamma = \frac{n_2\omega_0}{cS}, \tag{11}$$

is the nonlinear parameter in units of $W^{-1}m^{-1}$. Note that, in Eq. 11, S is the effective area of the beam such that the product $\gamma P_0$ scales with the laser's intensity.

Equation 10 is derived under the following assumptions: a linearly polarized beam, slowly varying envelope approximation, isotropic and nonmagnetic medium, negligible Raman response, frequency independent nonlinear index of refraction and neglect of dispersive terms higher than $\beta_2$ [1].

In general Eq. 10 can only be solved numerically and the split-step Fourier method [7] is the most popular method of doing so. However, in the lossless, anomalous dispersion regime ($\beta_2 < 0$) it is possible to solve Eq. 10 exactly for the case $\frac{\partial A}{\partial z} = 0$. In this situation, the nonlinear term of Eq. 10 balances the dispersive term to allow for long distance propagation without any changes to the temporal envelope of the pulse. These solutions can be observed in many physical systems and are referred to as solitons or solitary waves. Optical solitons have been found to play a vital role in supercontinuum generation in the anomalous dispersion regime since pulses undergoing a modulational instability tend to break into a series of soliton-like pulses [8].

Although Eq. 10 works very well for picosecond or longer pulses, this formalism falls short in predicting the details of supercontinuum generation. In order to fully model ultra-broadband processes one must consider higher order dispersive terms. Aside from dispersion, Eq. 10 does not include the Raman Effect or higher order derivatives of the nonlinear term (responsible for self-steepening and optical shock formation). The Raman response becomes increasingly important for ultrafast processes due to the fact that the bandwidth of these pulses overlap with the Raman gain spectrum allowing for so-called intrapulse Raman scattering.

Equation 10 can be adjusted to account for a Raman response by including in the formulation of $\chi^{(3)}$ a response function which is non-instantaneous,

$$\chi^{(3)}(t-t_1, t-t_2, t-t_3) = \chi^{(3)} R(t-t_1)\delta(t-t_2)\delta(t-t_3) \tag{12}$$

Where the two dirac-delta functions describe instantaneous processes and $R(t-t_1)$is the delayed or Raman response. Using Eq. 12 for the third order susceptibility the nonlinear polarization becomes,

$$\vec{P}_{NL} = \epsilon_0 \chi^{(3)} \vec{E}(\vec{r},t) \int_{-\infty}^{t} R(t-t_1) \left|\vec{E}(\vec{r},t)\right|^2 dt_1 \qquad (13)$$

By using Eq. 13 as the nonlinear response and by retaining higher order derivatives in the derivation of Eq. 10 we can derive a Generalized Nonlinear Schrödinger Equation (GNLSE):

$$\frac{\partial A}{\partial z} + \frac{\alpha}{2} A + (\textstyle\sum_n \beta_n \frac{i^{n-1}}{n!} \frac{\partial^n}{\partial t^n}) A = i\gamma (1 + \frac{i}{\omega_0} \frac{\partial}{\partial t}) (A(z,t) \int_{-\infty}^{\infty} R(t') |A(z,t-t')|^2 dt') \qquad (14)$$

If we assume that the electronic response (*i.e.* the Kerr nonlinearity) is instantaneous then we may approximate the response function as $R(t) = (1-f_R)\delta(t) + f_R h_R(t)$, where $f_R$ is the fraction of the nonlinear polarization attributed to the Raman effect and $h_R(t)$ is related to the Raman gain by $g_R(\Delta\omega) = \frac{\omega_0}{c n_0} f_R \chi^{(3)} Im(\tilde{h}_R(\Delta\omega))$ .

Equation 14 has proven to remain valid down to pulse lengths which are a single cycle of the electric field [8] and, therefore, can be applied to modeling extremely broadband processes such as supercontinuum generation.

The NLS of Eq. 10 and GNLSE of Eq. 14 can be simplified if we transform the temporal coordinate to move with the pulse. Using the definition $\tau = t - \beta_1 z$ Eq. 10 becomes,

$$\frac{\partial A}{\partial z} = -\frac{\alpha}{2} - \frac{\beta_2}{2} \frac{\partial^2}{\partial \tau^2} + i\gamma |A|^2 A \qquad (15)$$

while Eq. 14 takes the form of,

$$\frac{\partial A}{\partial z} = -\frac{\alpha}{2}A - \left(\sum_{n\geq 2}\beta_n \frac{i^{n-1}}{n!}\frac{\partial^n}{\partial \tau^n}\right)A + i\gamma\left(1 + \frac{1}{\omega_0}\frac{\partial}{\partial \tau}\right)\{(1-f_R)A|A|^2 + f_R A\int_{-\infty}^{\infty} h_R(\tau)|A(z,t-\tau)d\tau\,\} \tag{16}$$

In chapter 5 of this thesis we will present the results of simulations which were obtained by numerically propagating laser pulses using Eq. 16.

## 3. EXPERIMENT

### 3.1 Picosecond pulse amplification in the $CO_2$ gain medium

The difficulty of short pulse amplification in the $CO_2$ gain medium is that, at 1 atm of pressure, the bandwidth available for amplification can only sustain pulses which are nanoseconds in length. In the Neptune laboratory we increase bandwidth available for short pulse amplification by exploiting two broadening mechanisms: pressure broadening and field broadening [9]. Pressure broadening increases the bandwidth of the lasing transition due to the fact that, at high pressures, the collisional frequency becomes comparable to that of the radiative transition time. Figure 2 is a simulated gain spectrum of a $CO_2$ laser at 1, 10 and 25 atm of pressure. Here the individual rotovibrational lines are broadened by $\sim 3.5\ GHz/atm$ such that, at 25 atm of pressure, these individual lines overlap completely and the gain spectrum becomes smooth across the entire 1.2 THz bandwidth of the vibrational P branch.

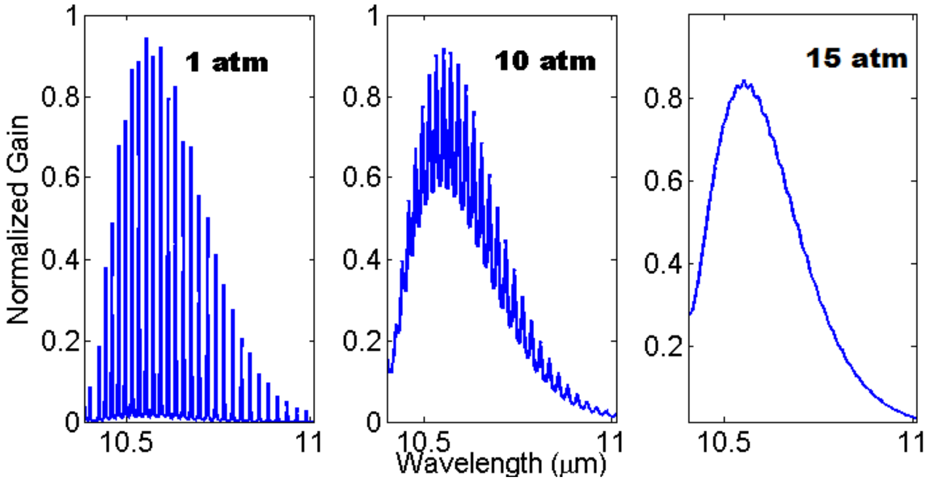

Figure 2: $CO_2$ gain spectrum at 1, 10 and 15 atm of pressure.

The bandwidth present at 15 atm of pressure would be ideal to amplify 3 ps pulses. Unfortunately, it is impractical to build discharge pumped amplifiers at these pressures unless the aperture of the laser is made prohibitively small. In practice these high pressure amplifiers operate at 10 atm of pressure resulting in a gain spectrum similar to the simulation result in figure (3b). When these 10 atm amplifiers are seeded with a picosecond pulse the output pulse is modulated in the frequency domain. The inverse Fourier transform of the output pulse's spectrum results in a pulse train in the time domain as depicted in figure 3.

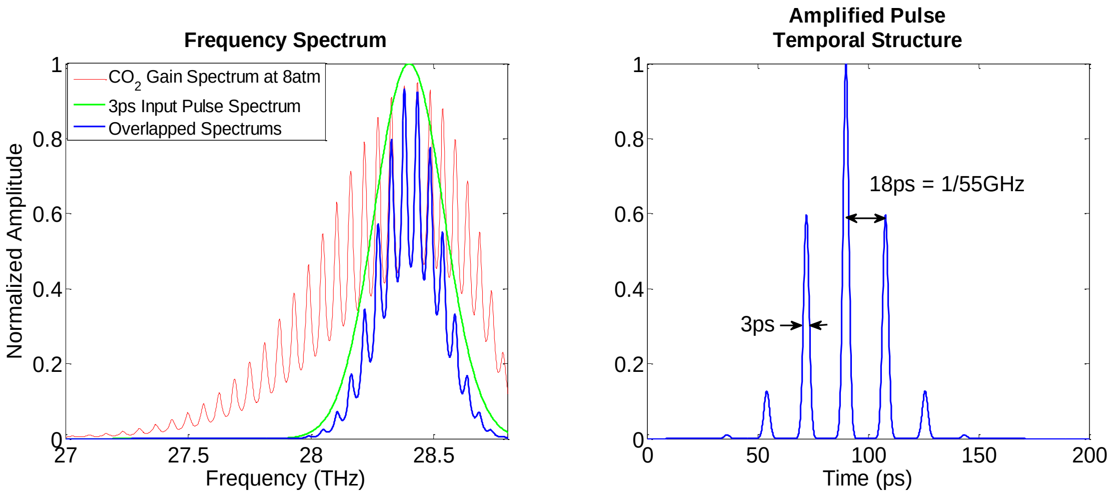

Figure (3): Simulation results showing the production of a pulse train in the time domain due to the residual 55 GHz modulation in the gain spectrum of a $CO_2$ laser at 10 atm of pressure.

This pulse train consists of several, 3 ps long pulses separated by 18 ps, a time scale related to the 55 GHz modulation in the gain spectrum.

The second broadening mechanism, field broadening, works in a way very similar to the ac Stark effect. When a strong electric field is applied to a quantum system the energy levels of the system are shifted in proportion to the electric field strength. If the driving AC field imposed on the quantum system in resonance with the system then this effect is called field broadening and can be used to broaden a lasing transition. The effect of field broadening can be approximated by $\Delta\nu_{Field} \approx 1.38 \cdot 10^7 \mu\sqrt{I_0}$ where $\mu$ is the $CO_2$ transition moment in Debye and $I_0$ is the peak laser intensity in $\frac{W}{cm^2}$ [9]. In general, the total broadening is a sum of both the pressure broadened and field broadened contributions, $\Delta\nu_{Total} = \Delta\nu_{Field} + \Delta\nu_{Pressure}$.

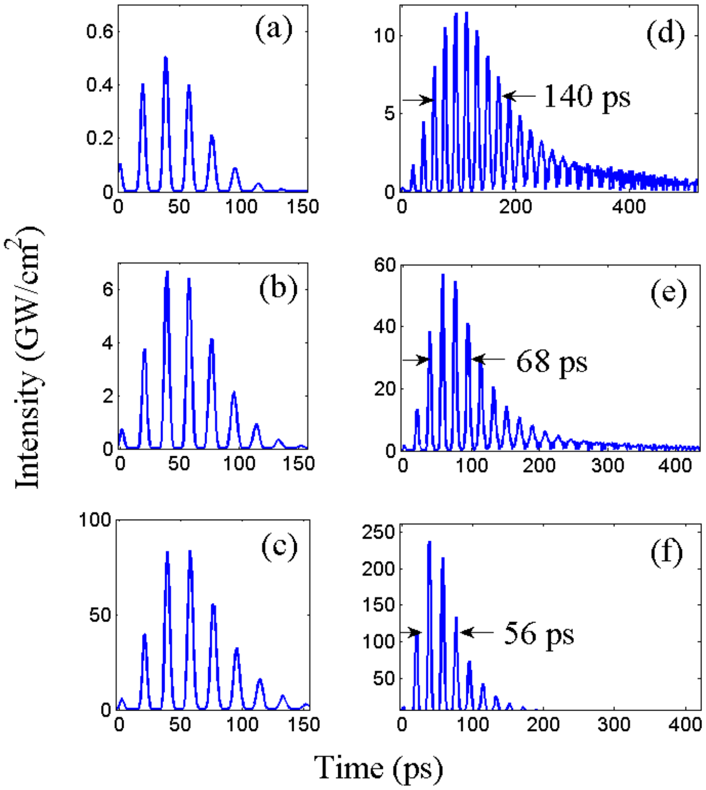

Figure (4): Simulation results showing the dependence of bandwidth on the field strength of the seed. (a), (b) and (c) are seed pulse trains with intensities of 0.4, 6 and 70 $GW/cm^2$, respectively. (d), (e) and (f) are the output pulses after amplification in a 3 m long inverted medium with a small signal gain of 3 $m^{-1}$ corresponding to seed pulses in (a), (b) and (c), respectively.

Using values of $\mu = 0.0275\ D$ [14] we find that, at peak intensities on the order $10^{10}\,\frac{W}{cm^2}$, a 1 atm $CO_2$ laser has comparable bandwidth to that of a 10 atm module. Figure 4 summarizes simulation results which demonstrate this effect. In the simulation laser pulse trains with an intensity of 0.5, 6.5 and 75 $GW/cm^2$ are amplified in 3 meter long, 1 atm $CO_2$ laser. From figure

4 it is apparent that the temporal envelope of the amplified pulse train decreases as we increase the seed's intensity. Thus production of a picosecond pulse train is a natural way to extract energy stored in the $CO_2$ medium in the high peak power regime of picosecond pulse amplification. This is why we use trains of 10 μm pulses in the experiment described below.

## 3.2 Description of the Laser System

The UCLA Neptune laboratory hosts a master-oscillator power-amplifier (MOPA) laser system which can nominally produce 100 GW, 3 ps, 10 μm, laser pulses at a repetition frequency of 1 Hz. Figure 5 is a block diagram of the system's front end where picosecond, 10 μm seed pulses are generated for further amplification. The $CO_2$ master oscillator consists of an intracavity low pressure $CO_2$ gain module, used to define a single longitudinal mode for the oscillator, combined with a 1 atm $CO_2$ TEA module. The output of the $CO_2$ master oscillator is a 200 ns, 10 μm, 30 mJ pulse. In order to produce picosecond pulses the 200 ns pulse is sliced by using a 3 ps 1 μm pulse as a gate for two optical switches. In the first switch the 10 μm and 1 μm beams are sent through a $CS_2$ Kerr cell place between two crossed polarizers [10]. During this interaction the 1 μm pulse increases the nonlinear index of refraction preferentially in the direction parallel to the polarization of the pulse. If the polarizations are set-up such that the 10 μm pulse is polarized $45^0$ relative to the 1 μm pulse then the 10 μm pulse will be rotated towards the 1 μm pump only when the field is present. This process results in the production of a 3 ps 10 μm pulse on the other end of the analyzer. The second switch is an n-type germanium slab which is oriented to transmit the 10 μm beam. When the 1 μm pulse is incident on the slab an electron-hole plasma is generated which is at a sufficient plasma density to reflect the 10 μm pulse. Here the germanium plate allows for a higher contrast than can be achieved with the Kerr cell alone. The reflected picosecond pulse is then collected and sent for further amplification.

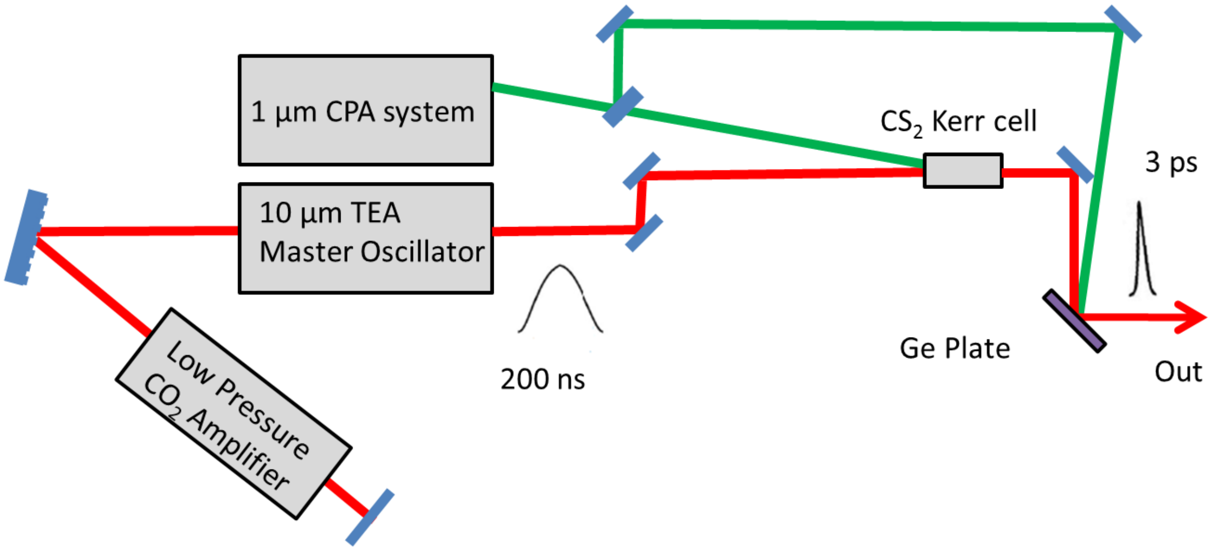

Figure 5: Block diagram depicting the production of 3 ps, 10 μm pulses from master oscillator.

Figure 6 is a block diagram of the Neptune Laboratory's amplifier chain where picosecond pulse amplfication is realized in two stages. In the first stage a few nJ seed pulse is amplified to tens of mJ in two 8 atm $CO_2$ lasers where the high pressure provides the bandwidth for picosecond pulse amplification. The first high pressure laser is used as a regenerative amplifier while the second high pressure laser is used as a double pass booster amplifier. It is in this first stage of amplification that the picosecond pulse train forms. In the second stage the pulse train, now having a peak power on the order of 2-5 GW, is amplified to 20 GW or hundreds of mJ in a TEA $CO_2$ module where the high field of the laser pulse provides the bandwidth for final amplification.

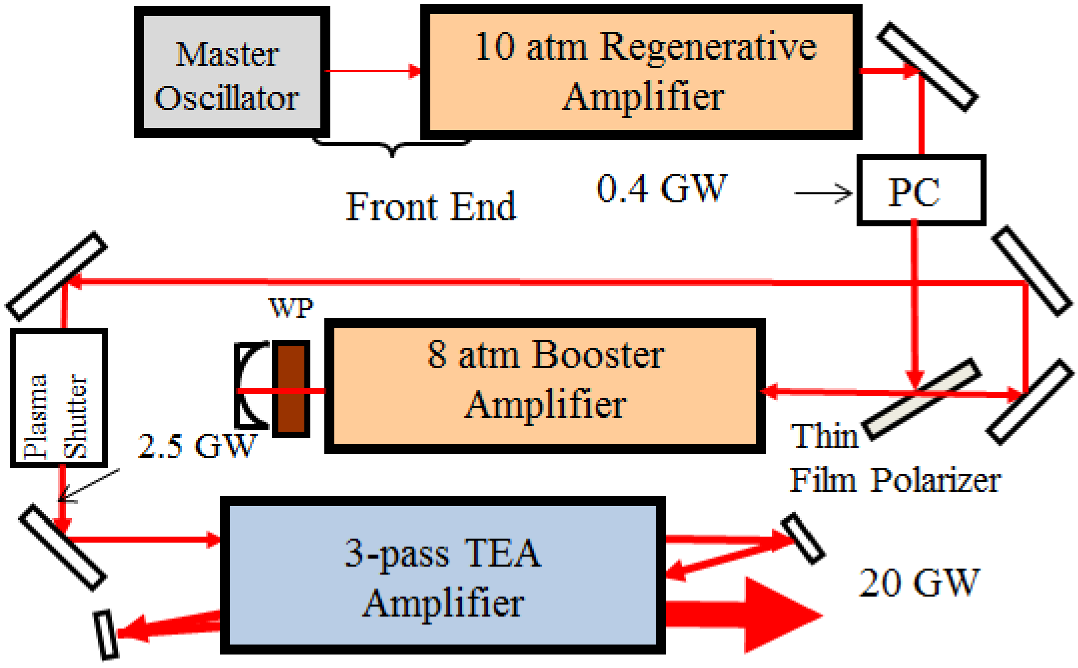

Figure 6: Block diagram of the Neptune Laboratory's amplifier chain. Orange blocks indicate parts of the chain which rely on high pressure of the active medium to sustain picosecond pulse amplification while blue blocks indicate parts of the chain that rely on field broadening.

Figure 7 depicts a temporal profile of the output pulse. Similar to simulation the pulse train consists of 3 ps pulses with a separation of 18 ps. The pulse train was measured with a streak camera by upconverting 10 µm radiation to 658 nm, additional details about this measurement will be discussed in section 3.6.

In the experiments described here we have only used the output of the laser chain after the second 8 atm amplifier in an effort to limit fluence on the surface of the GaAs crystal. For this configuration the peak power of the pulse train is approximately 2-5 GW while the temporal structure is similar to that shown in Figure 7.

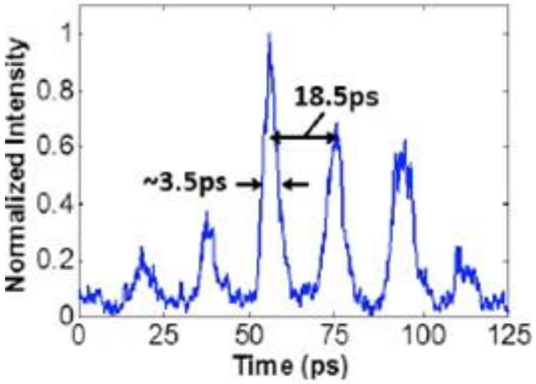

Figure 7: Temporal profile of the 10 µm picosecond pulse train as measured by a streak camera.

## 3.3 Description of the GaAs crystal

The GaAs crystal used in experiment is a 14 x 14 x 67 mm, AR coated crystal originally used as a Pockel cell. Figure 8 is a plot of the wavelength dependence of the group velocity dispersion of GaAs as measured in [11]. We can see from the figure that, at 10 µm, we are operating in the negative GVD region of the spectrum.

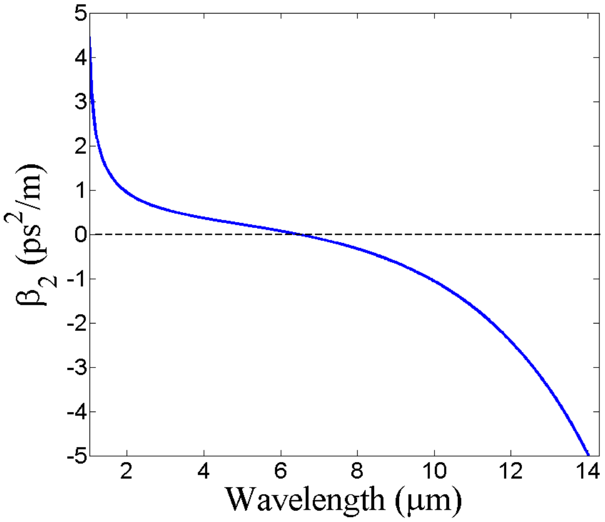

Figure 8: Group velocity dispersion versus wavelength for GaAs. At 10.6 µm GaAs has a negative GVD.

Using the dispersion measured in [11] we calculate a GVD of $\beta_2 \approx -2\ ps^2/m$ at 10 μm From [12] the nonlinear index of refraction in GaAs is, $n_2 \approx 2 \cdot 10^{-4} cm^2/GW$.

Aside from the dispersive and nonlinear properties of GaAs the next most important property is the Raman response. In GaAs the Raman frequency is related to the phonon band and figure 9 is a plot of measured  fluorescence [13].

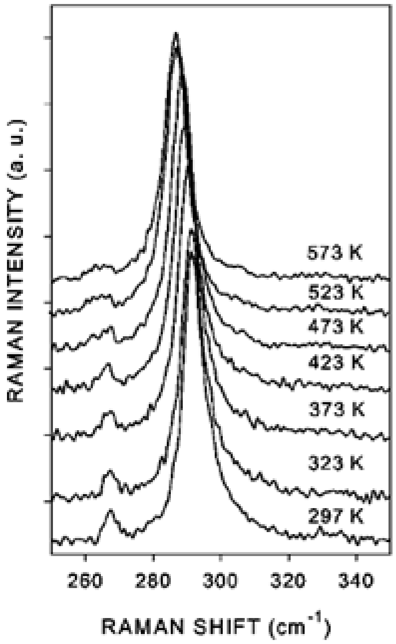

Figure 9:  Raman Fluorescence for various temperatures as measured in [13]

From figure 9 the Raman frequency shift is $\Omega_R \approx 292\ cm^{-1} \approx 8.55\ THz$ with an associated bandwidth of $\Delta\Omega_R \approx 3\ cm^{-1} \approx 1\ THz.$   For this Raman frequency we estimate using $\omega_{\frac{S}{AS}} = \omega_0 \mp \Omega_R$ that the Stokes and anti-stokes signals should be observed at ~ 16 and 8 μm, respectively.

## 3.4  Description of the experimental apparatus

To study supercontinuum generation in GaAs we have designed and built an apparatus to measure the temporal and spectral properties of the output radiation. Figure 10 is a simplified scheme illustrating the set-up of the experiment. The input radiation consists of 20 mJ, 3 ps $CO_2$ pulse trains which are focused using a reflective telescope to a beam diameter of 3-5 mm corresponding to peak intensities of $\sim 20\ \frac{GW}{cm^2}$. After focusing the light is coupled through the 67 mm GaAs crystal. The insert of figure 10 is the image of the beam profile after the crystal as measured by a pyrocam. During measurements the pyrocam was used to align the beam through the crystal and to ensure that there was no self-focusing. A small fraction (<1%) of the incident beam was used to monitor the pulse energy and was used for normalization.

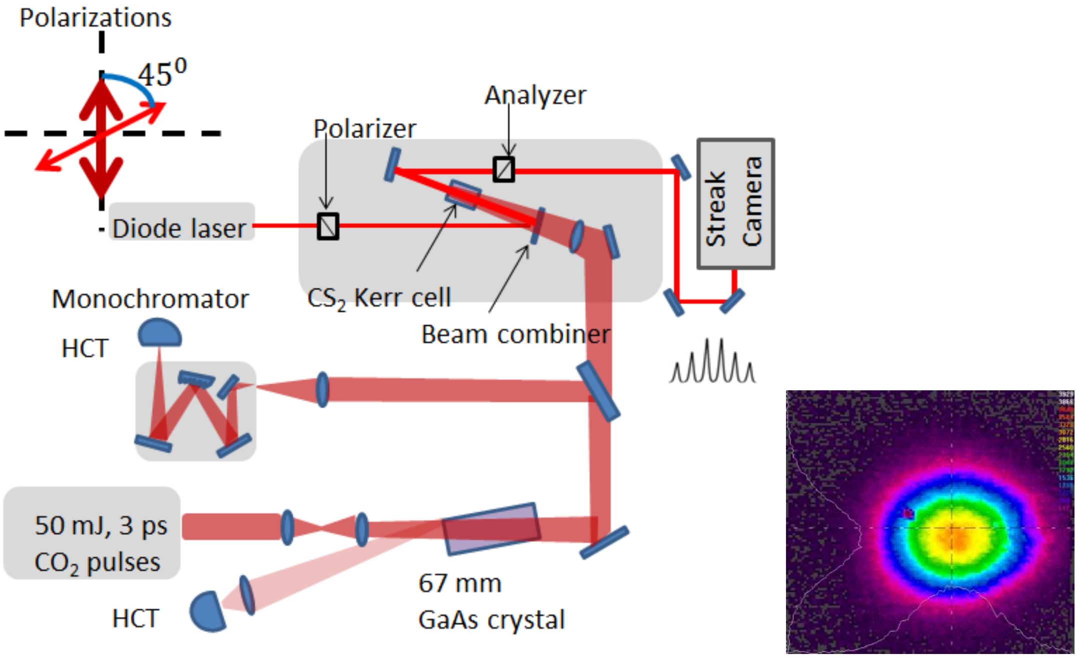

Figure 10: Simplified experimental set-up. The lower arm of the apparatus measures the spectral properties of the SC while the upper arm measures the changes in the temporal structure of the pulse train. In the figure HCT stands for HgCdTe detector. Insert: Pyrocam image of the beam profile in the crystal.

The supercontinuum radiation is transmitted through two optical arms. In the first arm the radiation is dispersed in a half meter long scanning monochromator for spectral measurements. In the second arm the radiation is upconverted to 658 nm and sent to a picosecond resolution streak camera in order to measure the temporal properties of the output radiation.

### 3.5 Apparatus for Spectral Measurements

Spectral measurements were performed using a Horiba iHR-550 scanning monochromator. Figure 11 is a photograph of our spectrometer configuration where the laser's path is indicated by a red line.

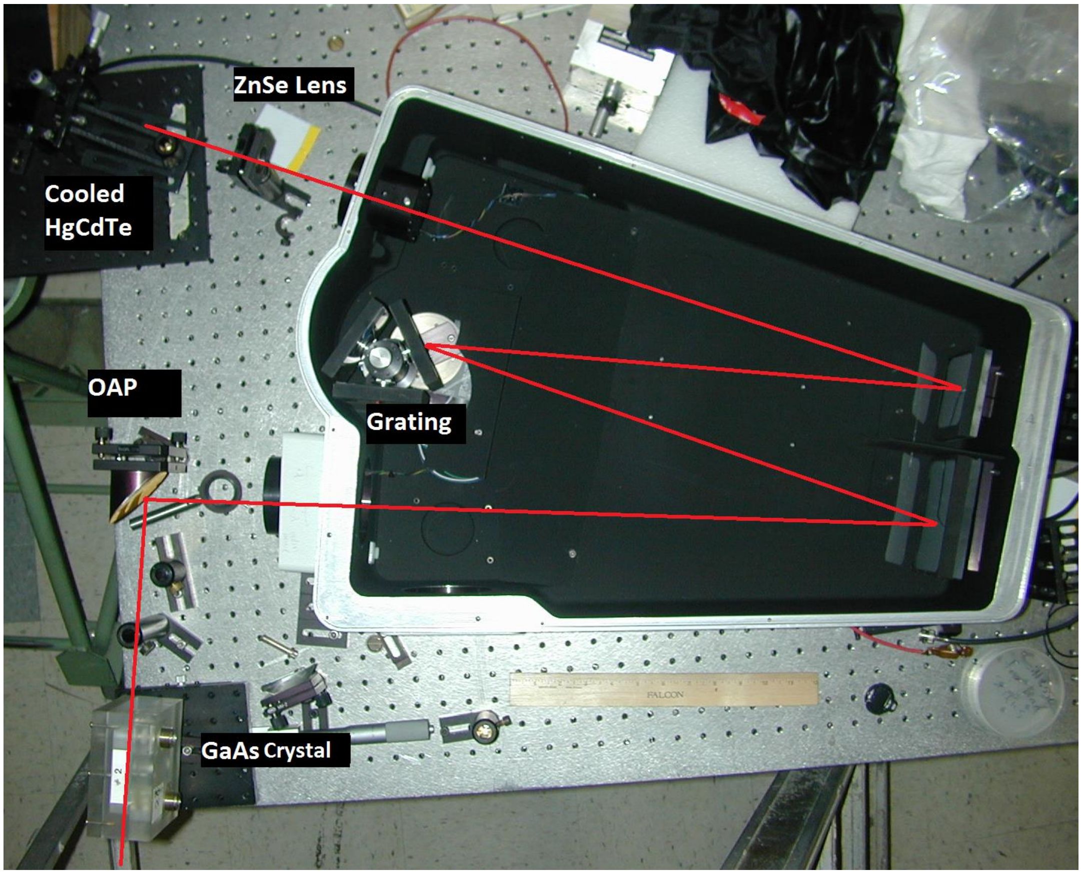

Figure 11: Set-up used to measure the supercontinua spectrum after GaAs.

After exiting the GaAs crystal, the beam was focused onto the input slit of the monochromator by using a 2'' diameter, 6'' focal length off axis parabolic mirror (OAP). In front of the input slit a 5 mm thick piece of polyethylene was used to attenuate the radiation by a factor of 100 in order to prevent plasma formation on the entrance slit. The spectrometer image relays the input slit to the output slit, both of which were open 1 mm during the measurement.

After the exit slit the beam was focused onto a 1 x 1 mm active area of the liquid $N_2$ cooled HgCdTe detector using a short focal length, 1" diameter, ZnSe lens. The detector was placed on an x-y translation stage in order to maximize the output signal. Due to the polyethylene attenuation of 100x and the spectrometer attenuation of approximately 1000x there was no need to attenuate the signal before the cooled HgCdTe detector for most data points. For those data points where attenuation was needed a 1 mm piece of Teflon of known spectral attenuation was used. The transmission as a function of wavelength for the Teflon attenuation can be found in the appendix.

The region of interest for this experiment was from 2 – 20 µm. Measurements from 6 – 20 µm were performed using a 50 G/mm diffraction grating blazed at 12 µm. Measurements from 2 – 6 µm were measured using a 150 G/mm grating blazed at 4 µm. Theoretical reflection curves for these two gratings can be found in the appendix. The spectral components very near to the carrier (~ 10 – 11 µm) were not measured to prevent damaging the detector. Each grating was roughly calibrated using a HeNe laser. An absolute calibration was performed during the measurements by using the second harmonic of the $CO_2$ laser (5.3 µm) for both the 150 G/mm and 50 G/mm gratings. Data points were measured in intervals of approximately 200 nm. All data presented here are an average of three shots, all of similar input energy as inferred from the back reflection HgCdTe detector.

Due to the sensitivity of the detector and the amount of energy used in the experiment, it was necessary to take precautions against stray light signals. In order to correctly measure the supercontinua spectrum a 10 μm broad band pass (BBP) and 10 μm notch filter were used to discriminate against stray light. BBP filters at $2\omega_0$ and $3\omega_0$ were also used to characterize the background light and it was found that light at the carrier frequency by in large dominated the false positive signals. The 10 μm light, although ubiquitous, was observed to be quasi-constant across the measured spectral range. This background was measured to be approximately -80 dB relative to the energy at the carrier frequency.

### 3.6 Apparatus for Temporal Measurements

The temporal structure of the output beam was measured using the Optronis SC-10 streak camera. Since the photocathode of the streak camera is insensitive to 10 μm radiation, the temporal information on the infrared beam was transcribed onto a 658 nm diode laser pulse by using the Kerr effect. Figure 12 illustrates the technique used to up convert the radiation transmitted from the GaAs crystal to 658 nm light. We first polarize the 10 μm and 658 nm beams such that the diode laser is polarized at $45^0$ from the $CO_2$ laser. We then co-propagate the 10 μm and 658 nm beams, the latter from a 30 mW diode laser, through a cell filled with $CS_2$, a liquid with large and relatively fast (~ 1 ps) nonlinear response [10]. In this $CS_2$ cell, the 10 μm beam pumps the nonlinear index of refraction and the 658 nm probe pulse witnesses this change in the refractive index and rotates towards to the pump.

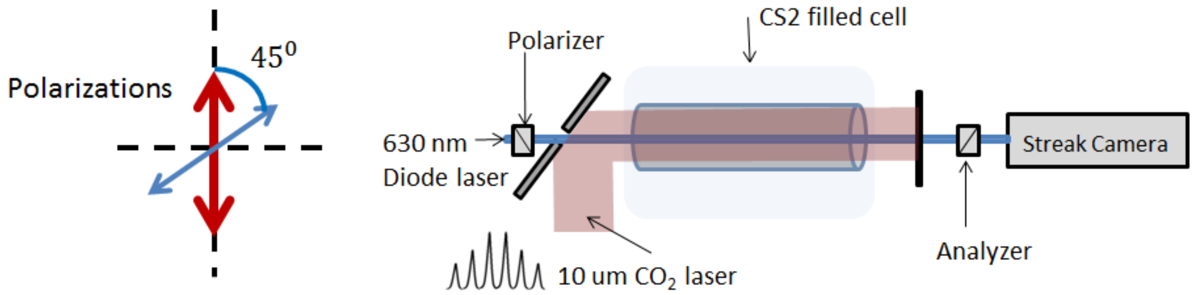

Figure 12: Diagram depicting the technique used to up convert the infrared SC radiation to 658 nm light

By using an analyzer set to block the un-rotated 658 nm laser, we are able to effectively transcribe the temporal information of the infrared pump onto the visible probe. In situation the transmission of the probe pulse is found to follow Malus's law [10]:

$$T(t) = Asin^2[2.34 \cdot 10^6 \left(\frac{\pi L}{\lambda}\right) n_2 I_{pump}(t)] \qquad (17)$$

During measurements the probe pulse is attenuated such that the transmission of the probe pulse remains on the quasi-linear portion of the sinusoidal curve of Eq. 17. It should be mentioned that, since Kerr effect based visualization requires rather high fields in the mid-IR, streaks presented here only correspond to those spectral components very near to the carrier (*i.e.* precisely those wavelengths close to the pump wavelength that were blocked on the spectrometer).

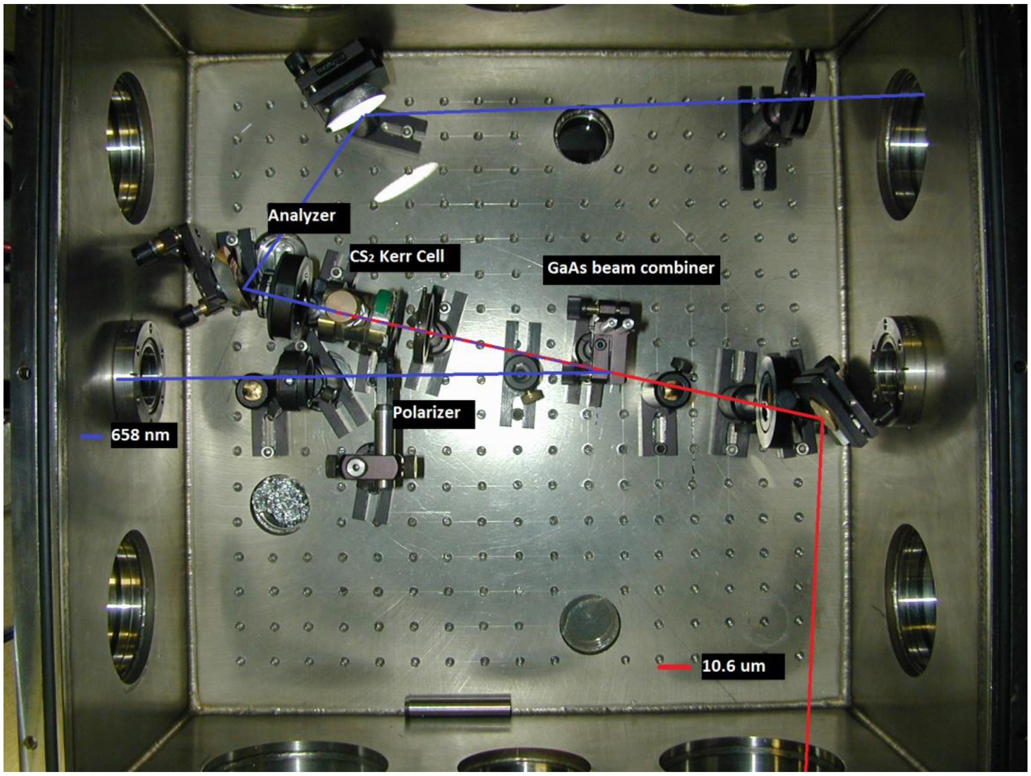

Figure 13: A photograph of the actual experimental set-up used for the temporal measurements in this thesis. Here the infrared pump is depicted by using a red line and the probe is depicted using a blue line. The probe beam is sent through a telescope and an analyzer set to polarize the beam at $45^0$ from the infrared beam. The two beams meet on a 500 μm wafer of GaAs which is used as a beam combiner. After the beam combiner the two beams are collinearly propagated through the $CS_2$cell where the first window of the cell is a 1” diameter NaCl plate and the second window of the cell is made of glass in order to dump the infrared beam and transmit the visible diode laser. The output analyzer was placed directly after the $CS_2$ Kerr cell in order to mitigate de polarization on the transport mirrors. After the analyzer the rotated diode pulse is sent to the SC-10 streak camera for the measurement.

## 4. RESULTS

### 4.1 Spectral Measurements after 67 mm of GaAs

Figure 14 is the measured spectrum after the $CO_2$ pulse train propagates through 67 mm of GaAs at a peak intensity of 20 $GWcm^{-2}$. The spectrum has been corrected for the spectral response of the attenuation, gratings and detector. The curves used to correct the spectrum can be found in the appendix.

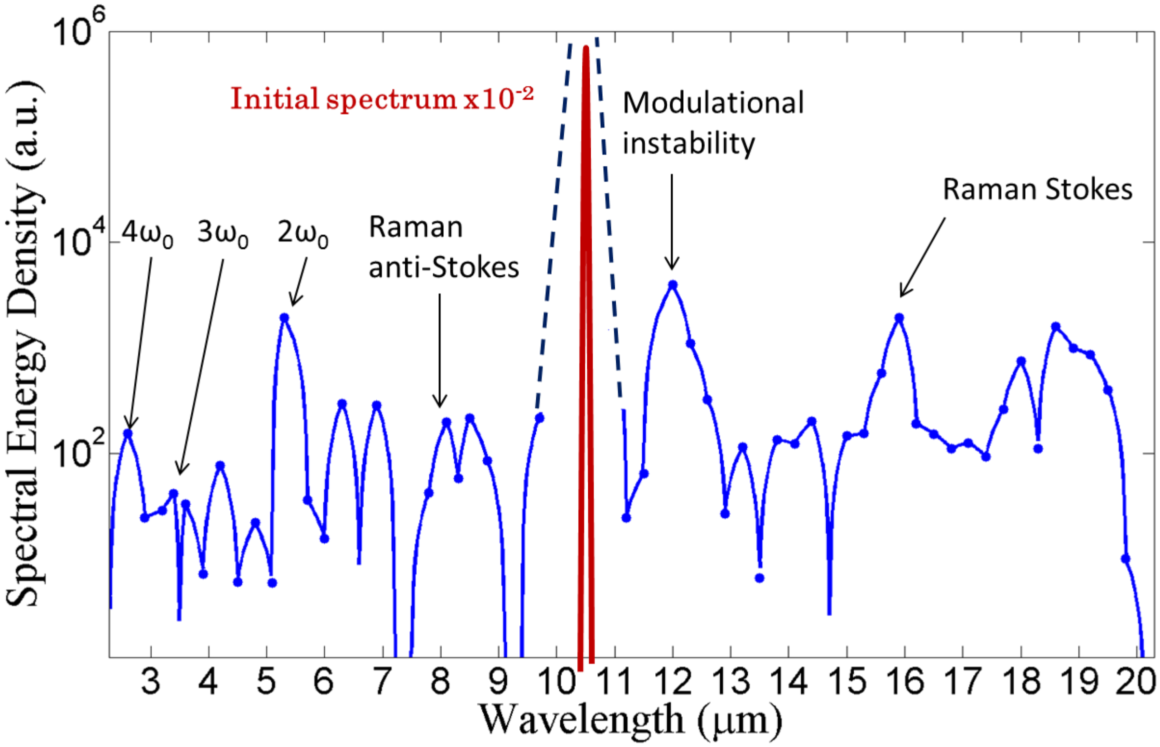

Figure 14: Spectrum after 67 mm of GaAs. The expected locations for peaks related Raman components, modulational instability and second, third, and fourth harmonic generation are labeled.

We observe a plateau-like spectrum at long wavelengths with a cut-off at 20 μm, attributed to the onset of strong absorption of the phonon band edge in GaAs. The red side of the curve also features a large peak at approximately 16 μm, a wavelength consistent with the Raman shift in GaAs. The blue side of the spectrum has a strong feature at 5.3 μm and a peak at 8 μm, the former corresponds to $2\omega_0$ generation while the latter corresponds to the anti-stokes component generated in GaAs.

We evaluated our conversion efficiency by sending the undispersed SC radiation through a narrow band-pass filter centered around 12.1 μm. We observe the conversion efficiency at 12 μm to be $10^{-5}$ relative to the carrier. Using this conversion efficiency we estimate that our Stokes and second harmonic signals have $\approx 10^{-5}$ relative intensity as compared to the carrier.

The harmonics are dominated by $2\omega_0$ light as we did not observe significant third or fifth harmonic yield. Although we suspected a significant contribution of $2\omega_0$ light from elements further upstream (*e.g.* NaCl windows on the regenerative amplifier), we were unable to measure any second harmonic signal above the noise with the GaAs crystal removed.

### 4.2 Temporal Measurements after 67 mm of GaAs

Figure (17) is a streak camera image of the $CO_2$ pulse train with the GaAs target removed. The time window is 200 ps on the streak camera. The insert of figure 15 is a lineout of the image; here we measure ~ 3 ps long pulses separated by ~ 18.5 ps, our usual pulse trains described in section 3.2.

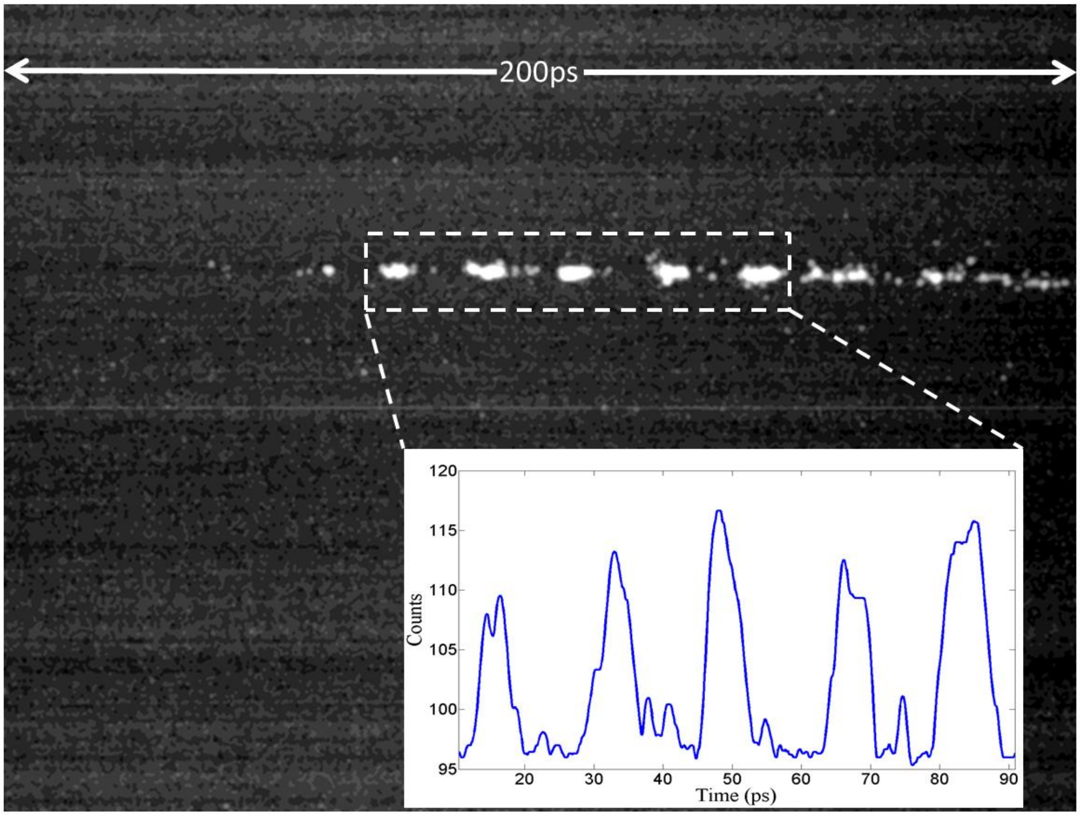

Figure 15: A streak of the $CO_2$ pulse train with the GaAs crystal removed.

Figure 15 is a streak of the pulse train after it propagates through 67 mm of GaAs. We observe that, after the GaAs, each pulse in the pulse train is strongly modulated. These pulses were measured to be approximately 1 – 1.5 ps, limited by the resolution of the streak camera, as compared to the 3 -4 ps time durations measured in figure 14. This observation is indicative that there is pulse splitting in the GaAs crystal, consistent with the calculated MI length of 5 – 7 cm in GaAs.

According to theory [7] when an optical pulse experiences a MI the initial pulse splits into a series of soliton-like pulses. Therefore these pulses should be sub picosecond, a time scale which is not measurable on our set-up due to the ps response time of the $CS_2$ Kerr cell and due to the measured 1.5 – 2 ps resolution of the streak camera. Analytic calculations (see section 2.6 ) using our experimental parameters predict that these pulses are hundreds of femtoseconds long. Chapter 5 of this thesis presents simulation results which are consistent with this estimate.

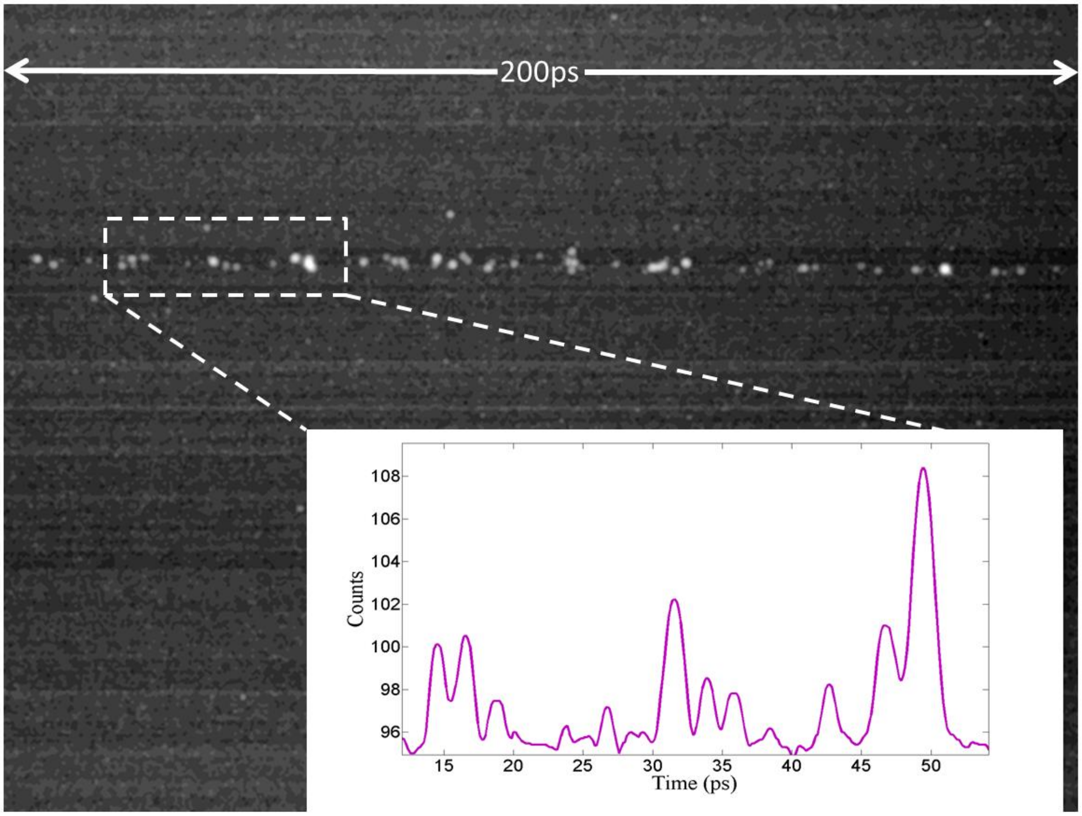

Figure 16: Streak image and line out of the temporal structure of the SC radiation. Each pulse is measured to be near the resolution limit of the set-up, ~1 ps.

We attempted to increase the yield of our SC generation by adding an additional 67 mm GaAs crystal (thereby doubling the interaction length). Interestingly, we observed that the yield on the plateau increased by only 20 - 30 %. This result is counter intuitive since the energy throughput is close to 100%. Perhaps very short pulses cannot drive the SRS process in an efficient way since the SRS response time in GaAs is on the order of 2 – 3 ps. Therefore the onset of MI in the first crystal should act to clamp the SC generation process in the second crystal.

It is important to note that we repeated these temporal measurements with a 2 mm GaAs crystal and did not observe any pulse break up.

## 5. SIMULATIONS AND DISCUSSION

To model SC generation in GaAs we have used a variation of the split-step Fourier method [7] to propagate the laser pulse using the one dimensional GNLSE of Eq. 16. The dispersion of GaAs was taken from [11], where we have included up to the fourth term in the Taylor series expansion ($i.e.\ \beta_4$). The Raman response for GaAs was modeled as an exponentially decaying sinusoid which was designed to match the Raman properties of GaAs as described in section 3.3 [13]. We have used a value of $f_R = 0.18 - 0.3$ in Eq. 16 and found that $f_R = 0.25$ gave the closest match to experimental observations. Note that $f_R$ is 0.18 for fused silica [8]. The model neglects harmonic generation, cross phase modulation and plasma contributions to the nonlinear susceptibility.

To understand the contribution of the $CO_2$ picosecond pulse train we have simulated the propagation of both a single picosecond pulse and a train of 3 ps pulses which closely resembles the pulse structure used in our experiment. Further, we have studied the contribution of SRS to the output spectrum by numerically disabling the Raman response.

### 5.1 Simulations of SC generation in GaAs using ps $CO_2$ pulse trains

We have modeled the propagation of an intense $CO_2$ pulse train through 67 mm of GaAs. Figure 17 shows the input spectrum and temporal profile of the pulse train. Similar to the experimentally measured pulses, our pulse train consists of 3 ps pulses separated by 18.5 ps. The most intense pulse in the train is initialized such that it has a peak power of 350 MW and nonlinear gamma factor of $\gamma = 5\ GW^{-1}cm^{-1}$. This value is consistent with an intensity of $3\ GW/cm^2$ and a Kerr index of, $n_2 = 1.7 \cdot 10^{-4} \frac{cm^2}{GW}$ [12].

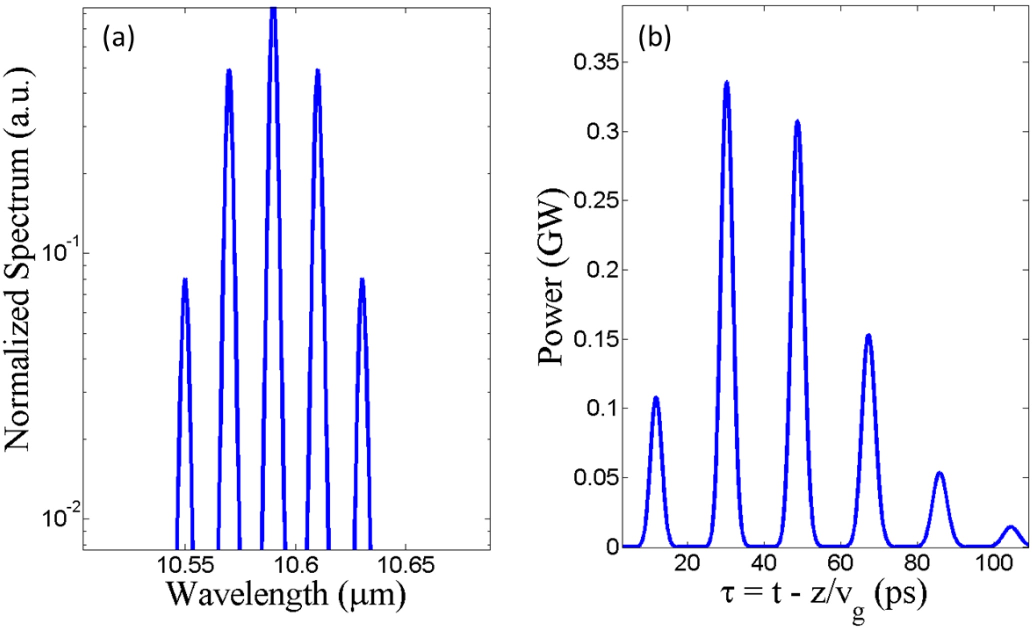

Figure 17: (a) Initial spectrum of the 10 μm pulse train. (b) Initial temporal profile of the 10 μm pulse train.

Figure 18 is the spectrum and temporal pulse profile after propagating through a 67 mm long GaAs crystal. The total spectral broadening is from 4.5 – 20 μm and contains two peaks at 8 and 16 μm related to SRS in GaAs. It is apparent that, the spectrum consists of many lobes which are indicative of a MI contribution to the spectral broadening. Indeed, in the time domain, the two most intense pulses in the pulse train exhibit strong modulation (see figure 18b)

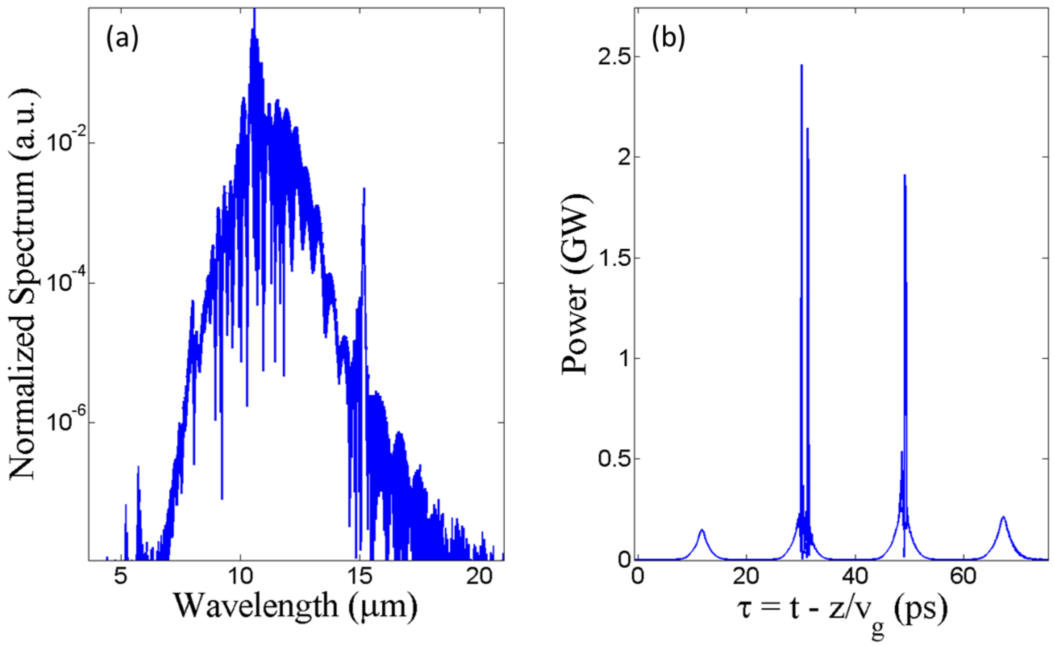

Figure 18: (a) Spectrum and (b) temporal structure after an intense $CO_2$ pulse train propagates through a 67 mm long GaAs crystal.

Figure 19 is a plot which depicts the evolution of the laser's frequency spectrum and pulse profile as it propagates through the crystal. For all such plots presented in this chapter, distance in GaAs is plotted along the vertical axis while frequency/time is plotted along the horizontal axis. The spectral evolution is plotted on a log scale while the temporal evolution is plotted on a linear scale. Note that the total broadening in figure 19 extends from 15 – 65 THz or from 4.5 - 20μm.

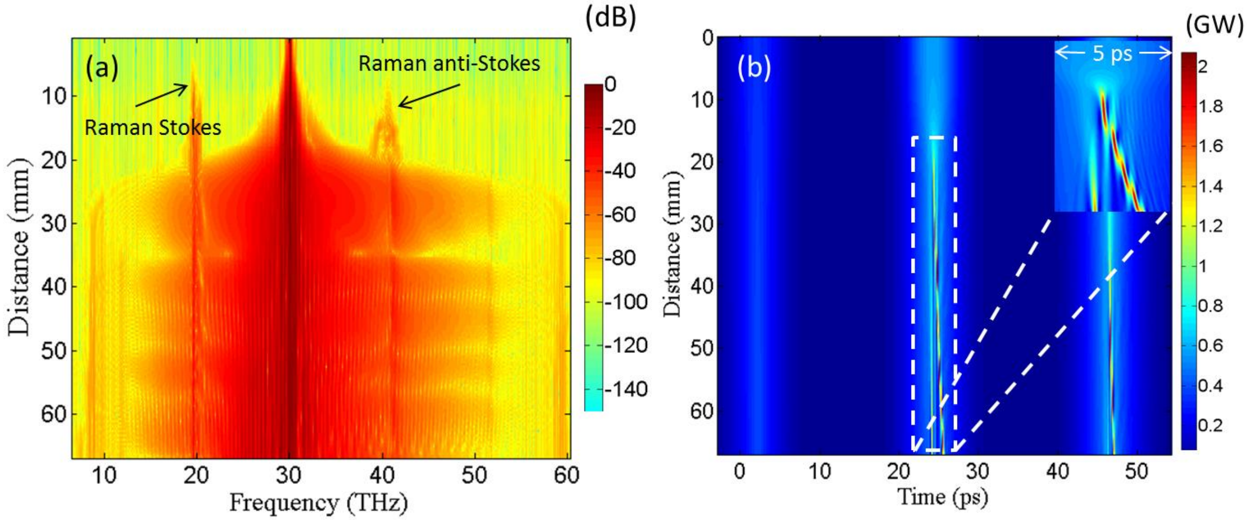

Figure 19: Plots of the (a) spectral and (b) temporal evolution of a 3 ps pulse train propagating through a 67 mm long GaAs crystal. Insert: Zoomed image of the most intense pulse in the time domain.

Figure 19 shows a spectrum with a width that oscillates along the propagation direction. The oscillatory behavior of the spectrum is correlated with cycles of compression and expansion of the pulses in time. These cycles of compression can be seen from the insert of figure 19 ( to see the correlation between the spectral and temporal evolution the reader is directed to the evolution of the single pulse simulation presented in figure 23). This cyclical evolution is a typical behavior of soliton like propagation of an optical pulse through a nonlinear medium with a negative GVD [7]. Also evident from the insert of figure 19 is that the two most intense pulses are delayed. This delay is the result of intrapulse Raman scattering and the negative group velocity dispersion of GaAs.

To demonstrate the role of SRS we repeated the above simulation with Raman scattering disabled. Figure 20 depicts the final spectrum and temporal pulse profile of the SC radiation.

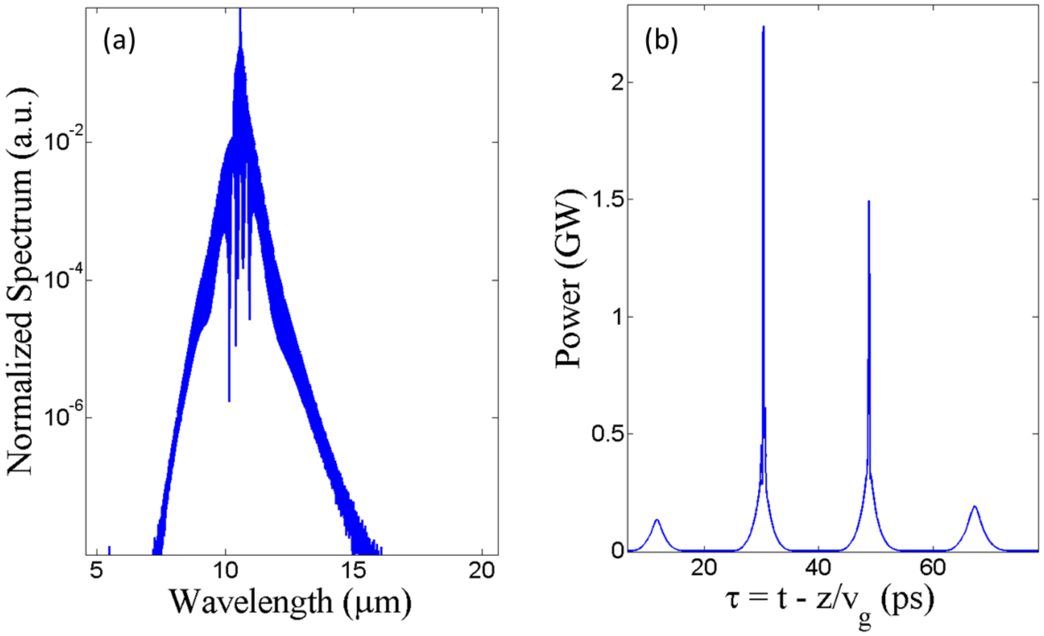

Figure 20: (a) Simulation of the final spectrum and (b) time domain after the pulse train propagates through 67 mm of GaAs with the Raman Effect disabled.

When SRS is disabled the low frequency cut-off is limited to 15 μm and both the Raman components and the lobe structure present in figure 18 are absent. Although the temporal pulse profiles are compressed, in these simulations there is no pulse splitting without SRS.

Figure 21 is a plot which depicts the spectral and temporal evolution of the pulse inside the GaAs crystal with SRS disabled. There is still an oscillation in the spectral width and temporal pulse profile although it has a longer period as compared to the case with SRS enabled. As can be seen from the insert in figure 21 the most intense pulse is no longer delayed as it compresses nor does it split into a series of pulses. It should be noted that in both the SRS enabled and SRS disabled simulations the pulse is compressed to approximately 300 fs or 10 cycles of the electric field.

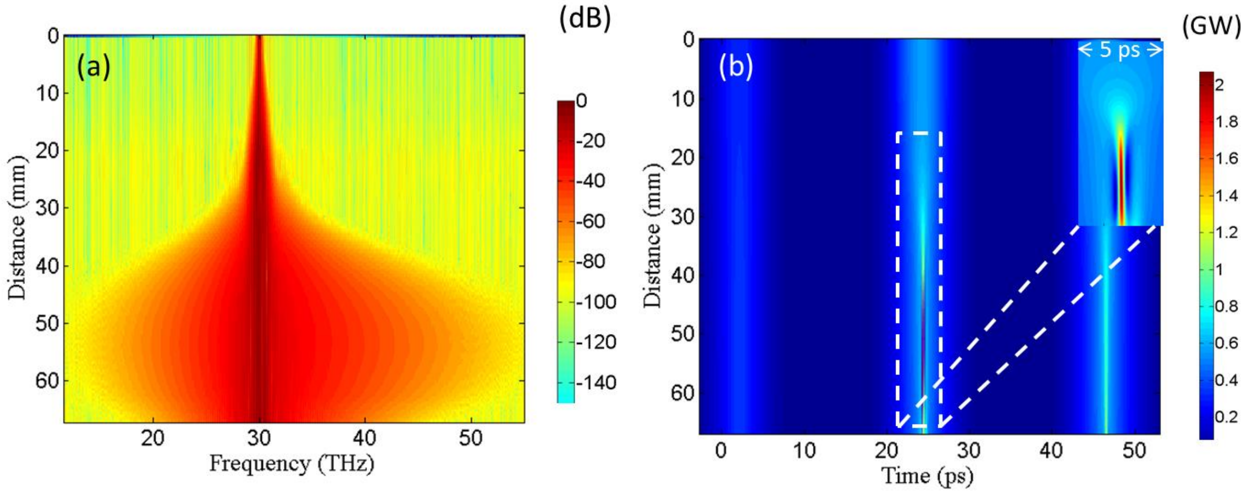

Figure 21: Plots of the (a) spectral and (b) temporal evolution of a 3 ps pulse train propagating through 67 mm of GaAs. The Raman effect was disabled for this case. Insert: Zoomed image of the most intense pulse in the time domain.

## 5.2 Single Pulse Simulations

To understand the role of the pulse train we have performed simulations of a single picosecond pulse having the same intensity as the most powerful pulse in the pulse train as shown in figure 22b. The initial pulse has a FWHM pulse length of 3.5 ps.

Figure 23 is a plot of the evolution of the laser's spectrum and pulse profile as it propagates through the crystal. As was the case with the pulse train simulations, both the time and frequency domain oscillate as the pulse propagates. In the single pulse case, the Raman contribution and total extent of the spectral broadening is from 17 -50 THz, less than

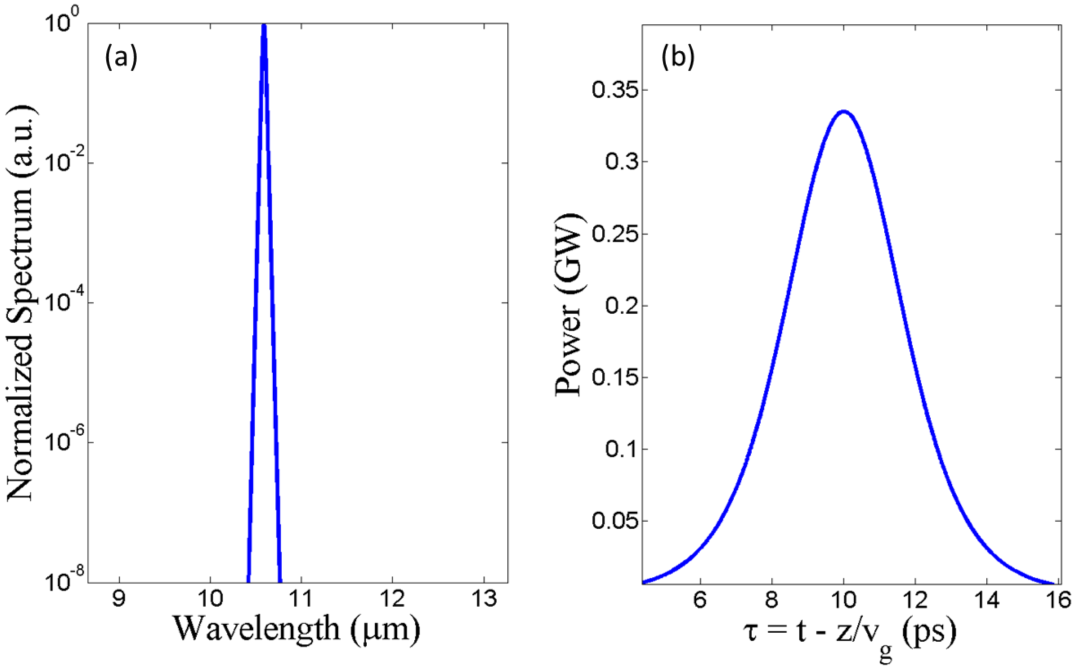

Figure 22: (a): Initial spectrum of the single 10 μm pulse. (b): Initial temporal profile of the 10 μm pulse.

with a pulse train. The most striking difference between the evolutions of the pulse train depicted in figure 19 versus the evolution of the single pulse depicted in figure 23 is the Raman components. In the single pulse case the Stokes line is weak and the anti-Stokes line is missing altogether whereas, in the case of the pulse train both Raman components offer a significant contribution to the spectrum.

We also simulated the propagation of a single picosecond pulse with the Raman effect disabled. In this case the result was similar to what is plotted in figure 21 although with less spectral broadening.

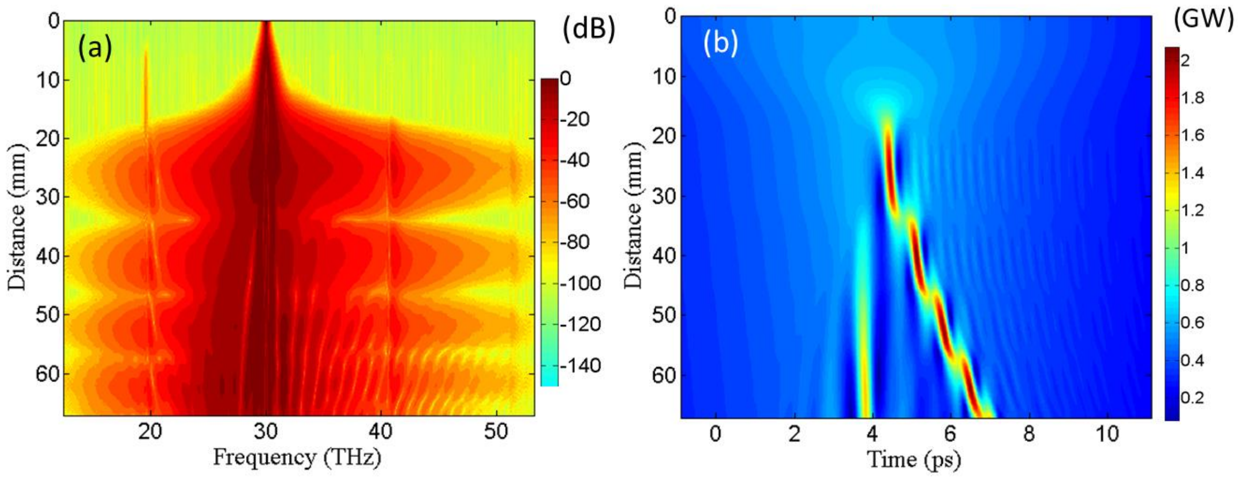

Figure 23: Plots of the (a) spectral and (b) temporal evolution of a 3 ps single pulse propagating through 67 mm of GaAs.

## 5.3 Discussion

The simulation results for the ps pulse train depicted in figure 18 show features which are in good qualitative agreement with that observed in experiment. The calculation predicts well the relative yield of the Stokes and anti-Stokes radiation along with pulse splitting in the time domain. Additionally, the calculation produces a similar total spectral broadening and long wavelength cut-off as compared to the measured spectrum in figure 14. The main discrepancy between experiments and simulations is a much lower measured SC generation efficiency.

The first limitation in our modeling is that, unlike propagation in a fiber, our situation is significantly impacted by three dimensional effects. For example, the simulated power was reduced to ~ 30% of the power measured in experiment due to the fact that we simulate a 1-D plane wave as opposed to a real Gaussian beam.

Another significant limitation in the modeling is that we do not account for harmonic generation. The exclusion of harmonic generation causes disagreement on the absolute yield for both the blue and red side of the spectrum. The blue side of the spectrum is not reproduced well because it is dominated by harmonics while the red side of the spectrum is affected since, in experiment, it is modified through FWM between the harmonics and Raman components.

One additional limitation in the modeling is that we neglect second order (*i.e.* $\chi^{(2)}$) processes. From the observed second harmonic yield it is clear that second order processes play an important role in SC generation in GaAs. Aside from second harmonic generation, second order processes may play an important role in the generation of the long wavelength plateau. For example, the experimentally observed peak at 18 μm (see Fig. 14) may be explained via difference mixing between the anti-Stokes and Stokes peak at 8 and 16 μm, respectively.

Despite these limitations, the simulations presented above have proven useful in a qualitative understanding of the physics of SC generation in 10 μm pumped GaAs. From the simulations, it is evident that stimulated Raman scattering plays an important role in increasing the spectral broadening. In the case where SRS was enabled it is intuitive that the pulse train should be more favorable for the production of a broad SC. Since the pulse train acts over ~ 100 ps and the Raman response time in GaAs is 2 – 3 ps one would expect that the Raman contribution and, in turn, the total spectral broadening should increase with the use of a pulse train. In this case, the pulse train is an ideal temporal structure as it combines intense pulses with a relatively long interaction time. It is this long interaction which allows us to generate anti-Stokes yield which is 10% of the Stokes yield when using a pulse train, as shown in figure 19.

The final interesting aspect of the simulations is that they predict the existence of an optimum interaction length before reaching saturation in the spectral broadening. Our experimental observation of saturation in the yield when using two crystals is qualitatively consistent with the simulated spectral evolution. This oscillatory behavior is similar to a class of solutions of the NLSE which describe the cyclical propagation of higher order solitons [7].

## 6. CONCLUSIONS

In this thesis we have described experimental results on SC generation in a ~7 cm long GaAs crystal pumped by 3 ps, 10 μm pulses. To the best of our knowledge, the observed 2 – 20 μm spectrum represents the record spectral broadening in the mid-IR range using nonlinear optical techniques. Observation of a long wavelength plateau and a strong Stokes signal indicates that Raman processes are responsible for the observed broadening. Further, time resolved measurements indicate that pulse break up caused by a modulational instability plays an important role in the generation of broadband light in GaAs.

Although the spectral broadening is impressive, our SC yield is still low compared to conversion efficiencies achieved in chalcogenide fibers [3]. We believe that the efficiency could be increased by a careful optimization of key parameters governing the interaction (*i.e.* intensity, pulse length and dispersion). Dispersion could be changed by using a GaAs waveguide where the waveguide contribution to dispersion is significant or by using shorter laser pulses. Unfortunately, it is difficult to increase the intensity above that used in experiment as we were operating very close the damage threshold of the AR coatings. Certainly our results suggest that there are limitations in mid-IR SC generation in the solid state, especially at a high repetition rate.

Future work will focus on studying similar nonlinear processes presented here but in gas filled waveguides that can be easily exposed to intensities from $10^9$-$10^{12}$ W/cm$^2$. The end goal is to develop an apparatus to control the spectral and temporal properties of our 1 Hz, 20 GW $CO_2$ laser system to study nonlinear optics and pulse chirping and compression in the mid-IR.

## Appendix

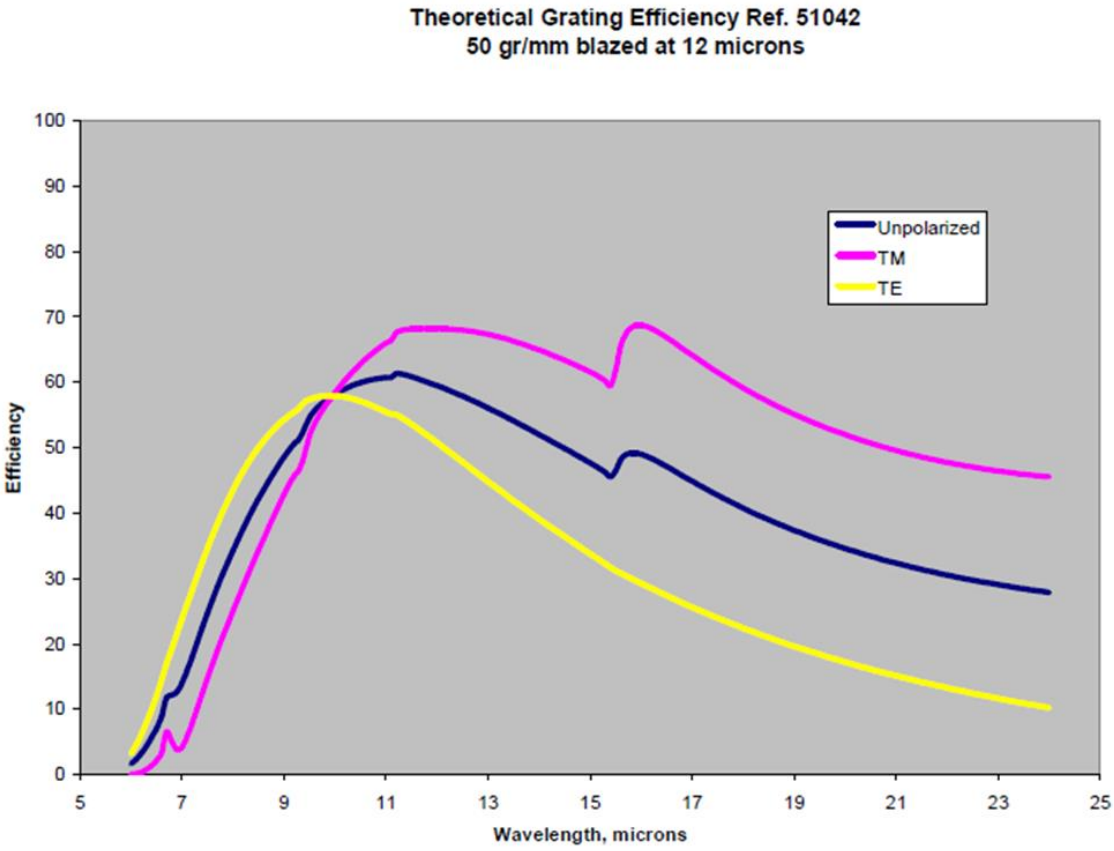

Figure A.1: Grating efficiency for the 50 G/mm grating used in the experiment. TM is tranverse magnetic and TE is tranverse electric.

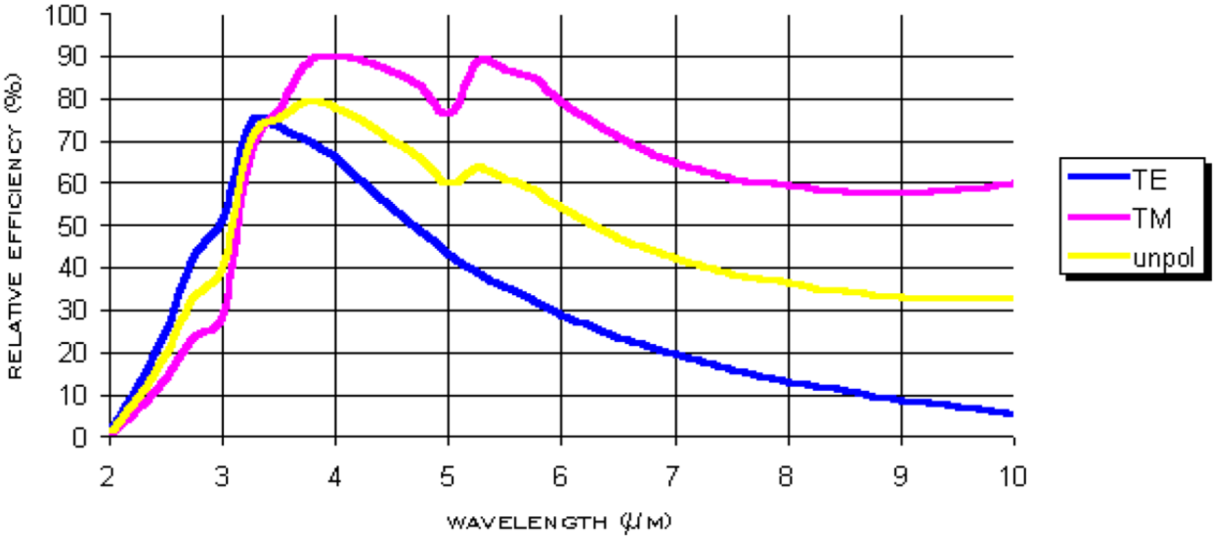

Figure A.2: Grating efficiency for the 150 G/mm grating used in the experiment. TE is transverse electric and TM is transverse magnetic.

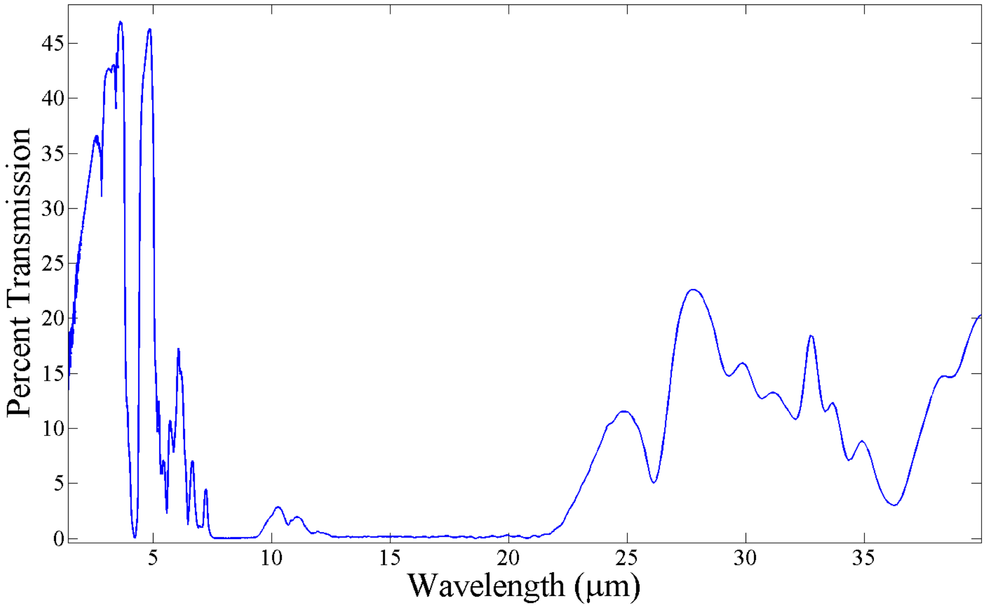

Figure A.3: Percent transmission versus wavelength for the 1 mm thick Teflon attenuator used in the experiment.

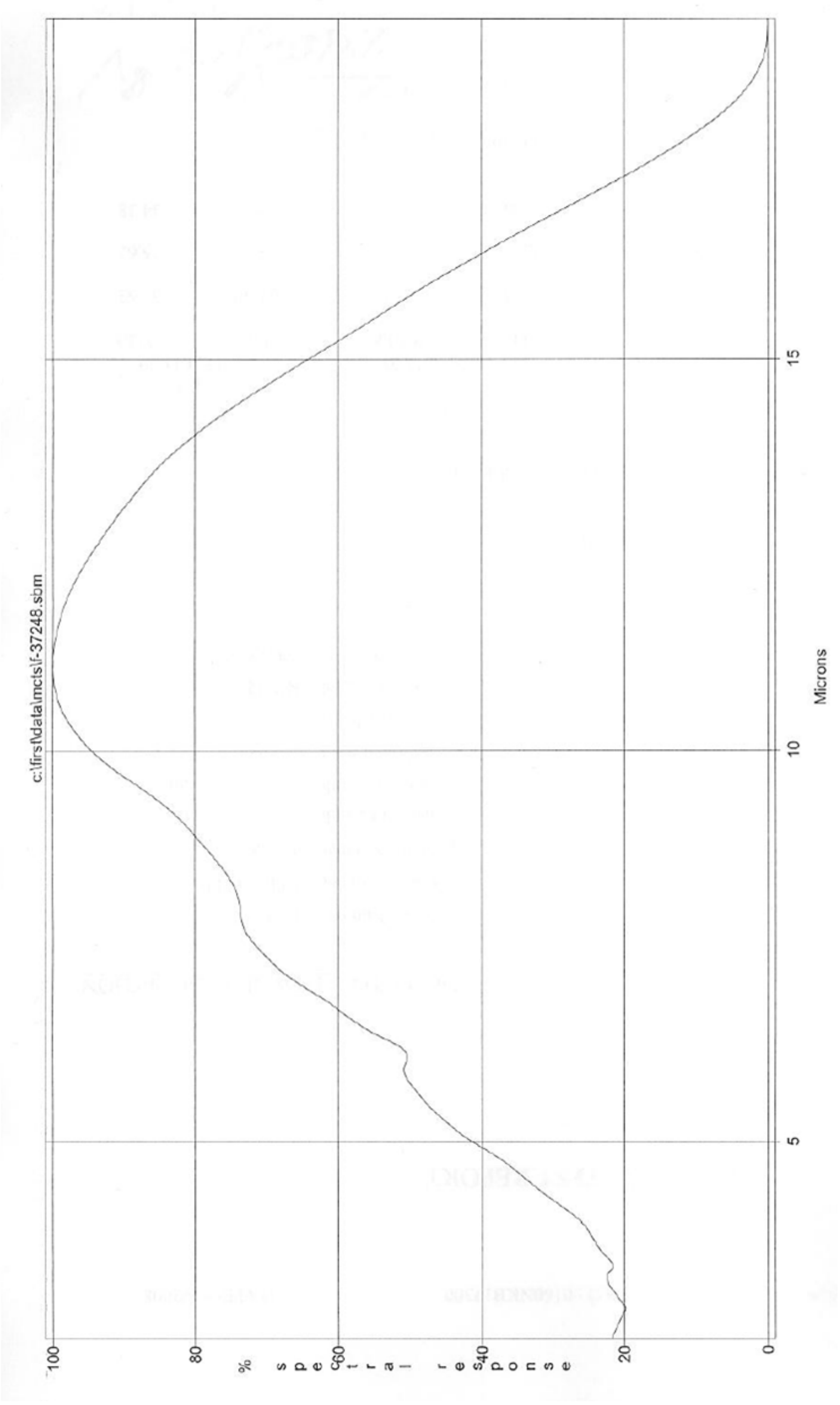

Figure A.4: Spectral response versus wavelength for the detector used in the experiment.

## References

[1] R.R. Alfano, *The Supercontinuum Laser Source*. Springer, New York (2006)

[2] R.R. Alfano and S.L. Shapiro "Observation of self-phase modulation and small-scale filaments in crystals and glasses". Physical Review Letters. Vol. 24, No. 11 (1970)

[3] C. Xia, *et. al.* "Mid-infrared supercontinuum generation to 4.5 μm in ZBLAN fluoride fibers by nanosecond diode pumping" Optics Letters, Vol. 31, No. 17 (2006)

[4] P.B. Corkum, P.P. Ho, R.R. Alfano, and J.T. Manassah. "Generation of infrared supercontinuum covering 3-14 μm in dielectrics and semiconductors." Optics Letters, Vol. 10, No. 12 (1985)

[5] I. Ahmad, L. Berge, Zs. Major, F. Krausz and S. Karsch.. "Redshift of few-cycle infrared pulses in the filamentation regime." New Journal of Physics. Vol. 10, 093001 (2008)

[6] K. Tai, A. Hasegawa and A. Tomita. "Observation of Modulational Instability in Optical Fibers." Physical Review Letters, Vol. 56, No. 2 (1986)

[7] G.P. Agrawal. *Nonlinear Fiber Optics*. Academic Press, New York (2001)

[8] J.M. Dudley, G. Genty and S. Coen. "Supercontinuum generation in photonic crystal fiber." Reviews of Modern Physics, Vol. 78 (2006).

[9] S. Ya. Tochitsky, J.J. Pigeon, D.J. Haberberger, C. Gong and C. Joshi. "Amplification of multi-gigawatt 3 ps pulses in an atmospheric $CO_2$ laser using ac Stark effect." Optics Express, Vol. 20, No. 13. (2012)

[10] C.V. Filip, R. Narang, S. Ya. Tochitsky, C.E. Clayton and C. Joshi. “Optical Kerr switching technique for the production of a picosecond, multiwavelength $CO_2$ laser pulse.” Applied Optics, Vol. 41, No. 18. (2002)

[11] T. Skauli, *et. al.* “Improved dispersion relations for GaAs and applications to nonlinear optics.” Journal of Applied Physics. Vol 94, No. 10. (2003)

[12] C.A. Kapetanakos, B. Hafizi, H.M. Milchberg, P. Sprangle, R.F. Hubbard and A. Ting. “Generation of High-Average-Power Ultrabroad-Band Infrared Pulses.” IEEE Journal of Quantum Electronics, Vol. 35, No. 4, (1999)

[13] A.M. Ardilla, *et. al.* “Temperature dependence of the Raman shift in GaAs conformal layers grown by hyride vapor phase epitaxy.” Journal of Applied Physics, Vol. 91, No. 8, (2002).

[14] R.K. Brimacombe and J. Reid, “Influence of the dynamic Stark effect on optically pumped 4.3 μm $CO_2$ lasers,” J. Appl. Phys. Vol. 58, No. 3, 1141-1145 (1985).